Materials & Design 253 (2025) 113916

Contents lists available at ScienceDirect

Materials & Design

journal homepage: www.elsevier.com/locate/matdes

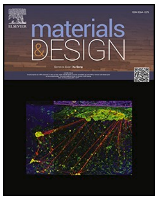

Superlubricity enabled by graphene nanocomposite film on carbon-coated AISI 1045 steel

Tabiri Kwayie Asumadu [a,b,d,e], Mobin Vandadi [d], Desmond Edem Primus Klenam [c], Kwadwo Mensah-Darkwa [a], Kwadwo Adinkrah-Appiah [b], Emmanuel Gikunoo [a], Nima Rahbar [d,*], Samuel Kwofie [a], Winston Oluwole Soboyejo [e,*]

[a] *Department of Materials Engineering, Kwame Nkrumah University of Science and Technology, Kumasi, Ghana*
[b] *Department of Materials Engineering, Sunyani Technical University, Box 206, Sunyani, Ghana*
[c] *Next Frontiers in Advanced Materials Lab, School of Chemical and Metallurgical Engineering, University of the Witwatersrand, 1 Jan Smuts Avenue, WITS, 2001 Johannesburg, South Africa*
[d] *Department of Civil Engineering, Worcester Polytechnic Institute, 100 Institute Road, Worcester, MA, USA*
[e] *State of University of New York Polytechnic Institute, College of Engineering, 100 17 Seymour Road, Utica, NY 13502, USA*

ARTICLE INFO

Keywords:
Macroscale superlubricity
Graphene nanocomposite film
Biowaste high temperature treatment
Raman spectroscopy

ABSTRACT

This paper presents a low-cost and innovative method for treating high temperature biowaste to create an ultra-low friction carbon-based coating on AISI 1045 steel. Utilizing carbon from Manihot esculenta biowaste, graphene variants were deposited on substrates at 500 °C and 900 °C. The microstructure and mechanical/tribological properties were studied pre- and post-treatment. These include Vickers hardness and wear characteristics that were measured with a ball-on-disk wear tester. Increasing treatment temperature and time resulted in high substrate hardness. The graphene variants were characterized using Raman spectroscopy with discernible trends D and G band trends. The I_{2D}/I_G and I_D/I_G intensity ratios varied as the treatment conditions changed. Electron backscatter diffraction, X-ray diffraction, optical, scanning electron, and atomic force microscopy provided insights into phases and microstructural features. Tribological tests showed remarkable ~95.20 % reduction with a superlubricious coefficient of friction of ~0.0015 and ~88 % decreased wear rate for substrates treated for 5 h at 900 °C. The graphene platelet and multiwalled defective structures on the substrates transformed into graphene oxide and graphene nanocrystals providing the needed solid lubrication. The underlying mechanisms are discussed before elucidating the implications of the result for the design of rigorous, novel carbon coatings for frictionless and ultralow-wear surfaces in a circular economy.

1. Introduction

Materials used in mechanical and electromechanical systems are susceptible to wear and energy losses due to friction. These systems are predominantly used in all engineering industries, for instance, the transportation and manufacturing industries use ~56 % of the energy produced globally annually [1]. Significant energy savings and prolonged material lifecycle can be achieved by reducing wear and friction on contact surfaces through surface engineering. Surface transformation methods with significant modifications of microstructure and composition are used to transform the surfaces of various engineering materials [2–5].

To reduce friction and wear, lubrication is investigated and applied in many mechanical systems [6–9]. However, these solid or liquid lubricants have introduced new challenges. Conditions such as high temperature and pressure renders liquid lubricants ineffective. This is because of associated issues like gas and waste pollution, flammability and thermochemical instability [10]. This has stimulated the development of solid lubricants that include two-dimensional materials like molybdenum disulphide and graphene. Variants of graphene such as carbon nano crystals, amorphous carbon, graphene oxide, carbon nanotubes, onion – like carbon, and nano diamonds have been essential for solid lubrication [11–16].

Variants of graphene have outstanding lubrication qualities [11–16]. These are due to incommensurable interacting surfaces and the formation and breaking of weak interlayer van der Waals bonds [17]. This

---

* Corresponding authors.
E-mail addresses: nrahbar@wpi.edu (N. Rahbar), soboyew@sunypoly.edu (W.O. Soboyejo).

https://doi.org/10.1016/j.matdes.2025.113916
Received 9 January 2025; Received in revised form 7 March 2025; Accepted 1 April 2025

Table 1
Average chemical composition of the As-received AISI 1045 steel.

Elem	C	Mo	Mn	Cu	P	Ni	Cr	Si	S	V
wt (%)	0.422 ± 0.002	0.037 ± 0.0001	0.67 ± 0.0045	0.168 ± 0.0006	0.013 ± 0.0005	0.098 ± 0.0032	0.167 ± 0.0002	0.196 ± 0.0015	0.031 ± 0.0001	0.024 ± 0.0001

mechanism is sufficient in interpreting the wear and friction phenomena at the micro- and nanoscales of graphene-like materials. Graphitic materials have been associated with superlubricious surface interactions. Superlow friction (superlubricity) normally refers to a domain of dynamic friction coefficient lower than 0.01 and heading towards 0.001 or less, advancing towards detectable limits of current tribometers [14]. Macroscale superlubricity with coefficient of friction ~0.004, enabled by graphene nanoscroll formation in between the mating surfaces has been reported [18].

Furthermore, the complicated surface morphology of heterogenous and homogeneous 2D materials, their compositional variations (from the macro- to nanoscales) and their effect on tribology are not completely resolved [19–25]. A typical example is graphene which has superior lubrication properties than graphene oxide at the micro- and nanoscales. However, the two materials at the macro-scale have excellent and comparable lubrication effects on metallic materials [16]. The mechanisms responsible for the similarity or differences are also not completely understood [14,16]. The scalability and cost implications of depositing graphene-like materials on large metallic surfaces are a cause for concern. This is partly due to specialized and expensive vapor deposition processes. Hence, these gaps provide opportunities for further research.

In this work, a novel and cost effective biotreatment process using "Manihot esculenta" biowaste (which has been successfully used as a carbon source for carbon-nitriding and graphene deposition in prior work, [26–30]) was used to deposit carbon nanostructures with graphene signatures on AISI 1045 plain carbon steel at 500°C and 900°C (for 3 h and 5 h). The 500°C temperature was chosen to experiment the

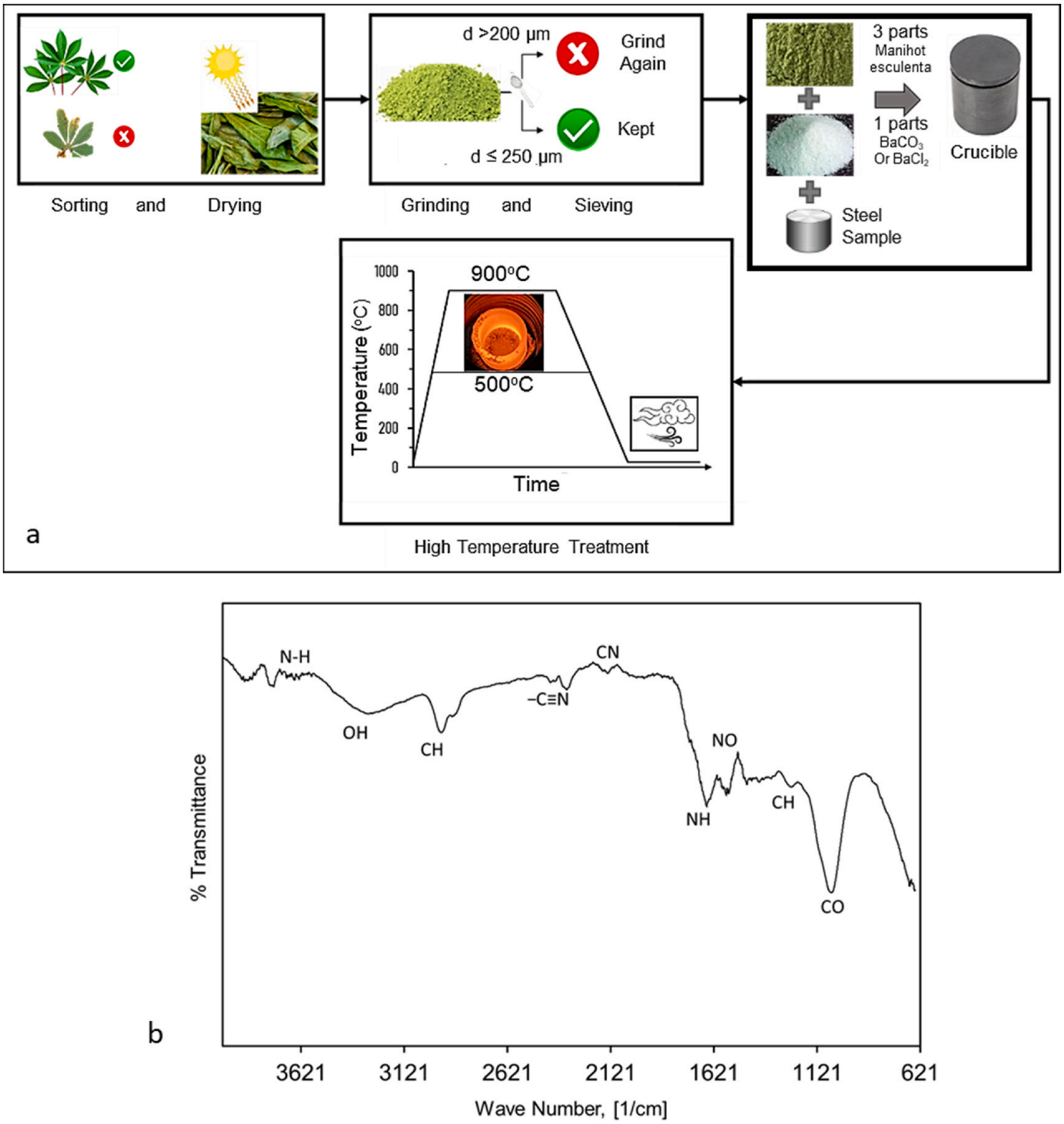

Fig. 1. (a) Schematic of the High-Temperature Biowaste Treatment of Steel Samples; (b) FTIR results of the Manihot esculenta biowaste powder.

possibility of depositing the carbon crystals at a lower treatment temperature as explored in prior work [31]. Carbon diffusion and case saturation, which is a precondition for multilayer graphene deposition has been achieved at 500°C for steels [32,33]. In our previous work, we demonstrated graphene deposition using this high temperature biotreatment method at 900°C on Ni, CPTi, Ti-6Al-4V and 1045 steel substrates [26]. High carbon diffusivity and case saturation with carbon are readily achieved at this temperature [34–36], which makes it an ideal temperature for depositing graphene variants. This current work presents the lowest coefficient of friction that has been achieved with this coating technique. It also focuses on steel as a substrate and present an in-depth understanding into the tribological behaviour. The possibility of depositing the coatings at a lower temperature (500°C) was also explored. This work presents the characterization of the carbon crystals deposited at 500°C and 900°C with a deposition time of 3 h and 5 h.. The hardness and tribological properties of the treated and untreated substrates were studied using a ball-on-disk wear test and micro-indentation, respectively. The multiscale microstructural features were also characterized using atomic force microscopy (AFM), scanning electron microscopy (SEM), electron backscatter diffraction (EBSD), energy dispersive spectroscopy (EDS), Raman spectroscopy, and optical microscopy. Temperature and duration of treatment effects (on case hardening, wear and friction properties of the substrates) were also evaluated. The graphene coatings were shown to result in lower wear rates and improved wear merit indices. The underlying mechanisms of friction and wear were also elucidated before discussing the implications of the current work for sustainable manufacturing within the context of a circular economy.

2. Materials and experimental methods

2.1. Material composition and sample preparation

AISI 1045 plain carbon steel rods of diameter of 18 mm were acquired from McMaster Carr, (Robbinsville, NJ, USA). Also, 18 mm diameter and 10 mm long substrates were sectioned using the Kalamazoo 13AW horizontal bandsaw (Kalamazoo, MI, USA) for the treatment. The cutting was done using a coolant to prevent any undesirable phase transformation during the sample preparation process. The Buehler AutoMet 250 Pro (Lake Bluff, IL, USA) was used to prepare the samples metallographically to 1200 grits before being subjected to the high temperature biowaste treatment.

The As-received AISI 1045 steel's chemical composition was verified by spark analysis with SpectroMaxx LMM-14 Glow Discharge Optical Emission Spectroscopy (GDOES)(Kleve, Germany). The results were analyzed in triplicate and the average compositions of the untreated steel are given in Table 1.

2.2. High-temperature biowaste treatment (HTBT) of steel substrates

The carbon source that was used for the high temperature treatment was extracted from biowaste prepared from "Manihot esculenta" The biowaste was processed into bio-cyanide powder by sorting, drying, and pulverizing to produce 200 ± 50 μm particle sizes. The activation agents used to accelerate carbon diffusion and deposition were $BaCl_2$ and $BaCO_3$. A $BaCO_3$ and bio-cyanide powder mixture (of ratio 3:1) was prepared for the HTBT process at 900°C. Another batch of $BaCl_2$ and bio-cyanide powder mixture (of ratio 3:1) was also prepared for 500°C treatment. The treatments were done using a cylindrical steel chamber with length of 200 mm, inner diameter of 77 mm and wall thickness of 3 mm. Three 1045 steel substrates and balls were treated for each test condition with ~622 g of the mixture (bio-cyanide powder plus the activation agents) for three and five hours, respectively. The biotreated samples were designated as 500 HTBT for those treated at 500°C and 900 HTBT for treatment at 900°C. Another set of samples were prepared and used as control, they were normalized at the same temperatures and times as the biotreated samples. These samples were designated as HT 500 3 h, HT 900 3 h and HT 900 5 h.

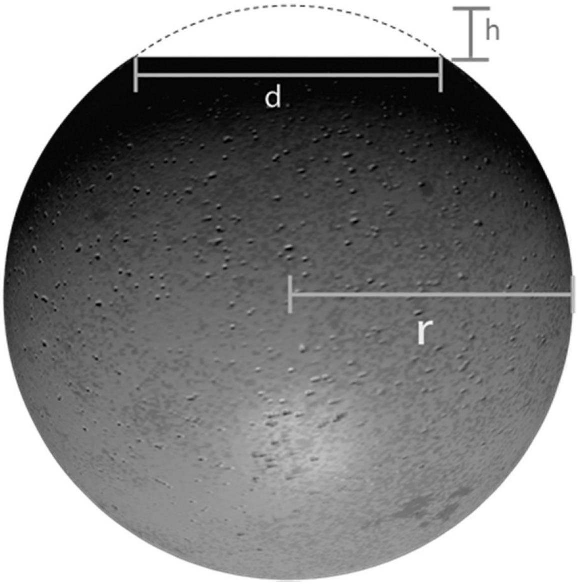

Fig. 2. Ball worn-out height Schematic illustration.

The high-temperature biowaste treatment method has been optimized and used for case hardening and deposition of carbon nano crystals with graphene signatures on Ni, CP-Ti, Ti-6Al-4V and 1045 steel substrates in our prior work [26,33]. A schematic illustration of the process flow associated with our innovative biowaste treatment method is presented in Fig. 1.

2.3. Friction and wear tests

The friction and wear properties of the treated and untreated substrates were measured using a calibrated ball-on-disk Anton Paar TRB^3 tribometer (Peseux, Switzerland). The load used was 2 N and it was applied on a substrate with a 6 mm diameter 100Cr steel ball as the counter body. The tests were conducted at 0.31 cm/s sliding speed (in triplicate per test condition) at room temperature in an environment with a relative humidity of 58 ± 4.23 %. Raman spectroscopy, SEM and EDS were used to characterize the wear tracks at various time intervals (the tests were paused, and the samples were carefully characterized). The wear track's depth was characterized using a Taylor Hobson Surtronic S128 Profilometer (Leicester, UK). Fig. 2 presents a schematic illustration of the ball worn-out height which was used to calculate the wear rates of the substrates. The height (h) was estimated using Eq. (1).

$$h = r - \sqrt{r^2 - \frac{d^2}{4}} \tag{1}$$

where d is the wear scar diameter of the ball and r is the ball radius.

The wear volume (V_b) of the ball and the wear volume of the coated and uncoated substrates were calculated using Eqs. (2) and (3) respectively. The treated and untreated substrates' wear rates (k_x) were then determined with Eq. (4).

$$V_b = \frac{1}{6}\pi h(3\frac{d^2}{4} + h^2) \tag{2}$$

$$V_w = A_w P d_{max} \tag{3}$$

$$k_x = \frac{V_w}{F \times s} \tag{4}$$

where Pd_{max} is the average penetration depth, A_w is the worn-out surface

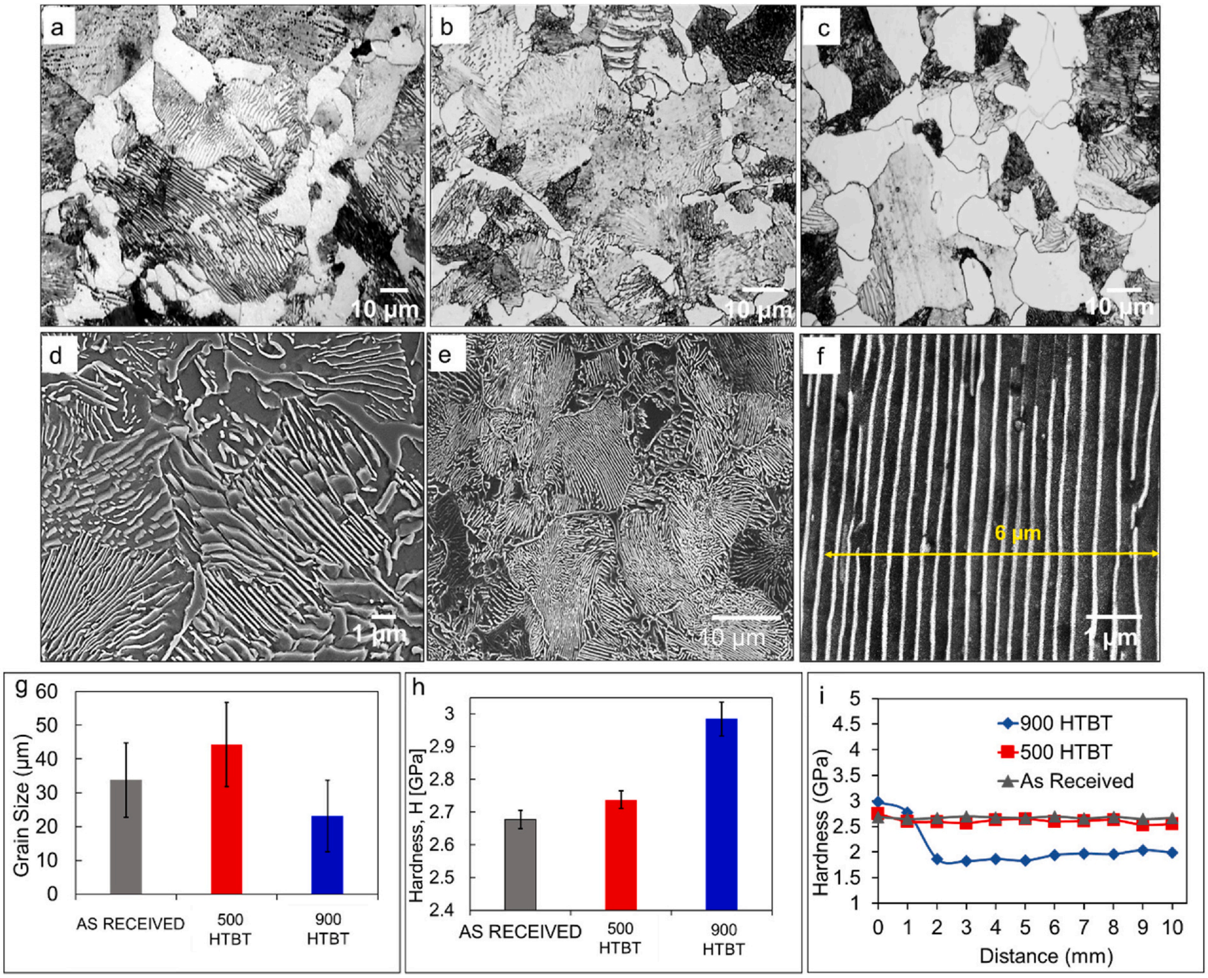

Fig. 3. Optical microscopy images, SEM micrographs, grain size analysis and hardness results of the cross-section of the treated and untreated substrates: (a) optical micrograph of the cross-section of As-received 1045 steel with proeutectoid ferrite and pearlite. (b) optical micrograph of the cross-section of the 500 HTBT substrates with coarsened pearlite grains in the microstructure, (c) optical micrograph of the cross-section of the 900 HTBT samples showing recrystallization of the ferrite phase in the microstructure (d) SEM image of upper bainite in the case depth of the cross-section of the 900 HTBT, (e) SEM image of conventional bainite below the upper bainite case, (f) lamellar spacing of the pearlite microstructure, (g) As-received 1045, 900 HTBT and 500 HTBT samples' grain size analyses, (h) hardness results of the surface of As – received, 500 HTBT and 900 HTBT substrates. (i) Microhardness profile of cross-section of the 900 HTBT substrates.

area, F is the applied load and "s" is the total sliding distance.

Triplicate temperature measurements for each condition were taken in between the mating surfaces using a Fluke 62 Max infrared thermometer (Fluke Corporation, Washington, USA). It has a distance-to-spot ratio of 10:1 with a single laser pointing system and a temperature measurement range of -30 °C to 500 °C. The ball-on-disk experiment stays the ball at a single location while rotating the disk (substrate). In this way the temperature of the disk drops immediately after the substrate leaves the ball's contact due to energy dissipation. The temperature measurements were taken in between the ball and the substrates at the points of contact. They were taken from three different experiments for each condition.

2.4. Micro-indentation hardness

The micro-indentation hardness was measured using a Wilson VH3300 hardness tester (Lake Bluff, IL, USA) with a Vickers conical diamond indenter tip. Loads from 0.3 to 50 kgf which corresponded to indentation depths 6–60 μm, were applied to the substrates with a 10 s dwell time. The hardness change in depth direction was from the surface into the matrix. The experiments were carried out in accordance with ASTM E2546-15 specifications. The indent diagonal was determined manually using an attached optical microscope. The hardness and the reduced elastic moduli (E_r) were estimated using Eqs. (5) and (6).

$$H = \left(\frac{P_{max}}{24.56h_c^2}\right) \tag{5}$$

$$\frac{1}{E_r} = \frac{1-\nu^2}{E} + \frac{1-\nu_i{}^2}{E_i} \tag{6}$$

where P_{max} is the maximum indentation applied load, h_c is the depth of indentation ν_i and ν are the Poisson's ratio for the indenter and indented material respectively. E_i and E are the Young's modulus of the indenter and indented material respectively.

2.5. Microstructural characterization

As-received and treated substrates were metallographically prepared. The as-polished surfaces were then etched with a 2 % nital for 12 s to reveal the microstructure. Optical microscopy was used to characterize microstructural features of the substrates with an SMZ800 N optical microscope (Melville, NY, USA). Further microstructural features of the treated and untreated substrates were then resolved with a JEOL JSM – 7000F Field Emission Scanning Electron Microscope (Golden, Co, USA) equipped with EBSD and EDS. The SEM images were captured in secondary electron mode with a voltage of 10 kV. The EBSD analyses was done using 20 kV, a step size of 5 μm and a tilt angle 70° to the sample's surface. The working distance was ~30 mm. Data on texture, grain size, phase fraction and crystal orientation maps were obtained.

The graphene-like deposits and the wear tracks were characterized with Raman spectroscopy. The spectra were obtained at ambient condition (22°C) using a Horiba XploRa Raman Micro Spectrometer (Kisshoin, Minami-Ku Kyoto, Japan) equipped with optical microscopy. The laser wavelength of 532 nm with an 1800-line grating, an aperture of 100 and a slit width of 300 was used for the acquisition of the data. A 100x lens was used to focus the laser light. The system was calibrated using a silicon wafer (1 0 0) with a peak of 520 cm^{-1}. The LabSpec 6 software accompanying the setup was used for the baseline correction and normalization.

The functional groups of the biowaste powder were characterized with the Fourier transform infrared (FTIR) spectroscopy. A Bruker vertex 70 Spectrophotometer with an attenuated total reflectance (ATR) mode (Billerica, MA, USA) was used for the spectra data collection. 1024 scans in the mid-infrared band of 4000 to 500 cm^{-1} were used. All measurements were done with a 4 cm^{-1} resolution.

Surface topographic analyses were done on the treated substrates using a Park Systems NX20 (Suwon, Korea) atomic force microscopy. The tests were performed in the non-contact mode with PPP-NCHR 10 M cantilevers using silicon nitride tips. The tips lengths ranged from 10 to 15 μm with a nominal radius of 10 nm per specifications from the manufacturer. A 1024 × 1024 pixels resolution was used for Image sizes of 25 × 25 μm and 5 × 5 μm at a scan rate of 0.17 Hz. The root mean square (RMS) roughness of the substrates' surface was calculated from Eq. (7).

$$R_{RMS} = \sqrt{\frac{1}{n}\sum_{i=1}^{n} z_i^2} \tag{7}$$

were z_i represents the height of the i^{th} pixel.

2.6. Hertzian contact analyses

Hertzian contact theory was used to assess the deformation and stresses under the counter body and the substrate. Eq. (8) was used to calculate the depth of indentation, u, while Eq. (9) was used to determine the contact area radius, "a" and E_r is the reduced elastic modulus is estimated from Eq. (10). Eq. (11) was then used to estimate the maximum stress s_{max} between the plane and the sphere. The estimated maximum stress from Eq. (11) was 224 MPa, and the indenter's contact area (determined with Eqs. (8)–(11)) was 52 μm^2.

$$u \approx \left(\frac{2P^2}{E_r^2 R}\right)^{\frac{1}{3}} \tag{8}$$

$$a \approx \left(\frac{3}{2}\frac{RP}{E_r}\right)^{\frac{1}{3}} \tag{9}$$

$$\frac{1}{E_r} = \frac{1}{2}\left(\frac{1-\nu_1^2}{E_1} + \frac{1-\nu_2^2}{E_2}\right), \tag{10}$$

$$\sigma_{max} = \frac{3}{2}\frac{P}{\pi a^2} = 0.4\left(\frac{E_r^2 P}{R^2}\right)^{\frac{1}{3}} \tag{11}$$

where P is the indenter load, R is the indenter radius, E_1, ν_1 represent the elastic moduli and Poisson ratio of the sphere and, E_2, ν_2 are for the substrate, respectively.

3. Results and discussion

3.1. Microstructure and crystallographic phase mapping

3.1.1. Cross-sectional microstructural characterization

The cross-sectional microstructural features of the as-received material and the carbon treated materials are presented in Fig. 3. The cross-sectional microstructure of the 1045 steel is the characteristic proeutectoid ferrite and pearlite. This is consistent with prior work [27,33,37,38]. The cross-section of the 500 HTBT substrates had shrunk proeutectoid ferrites due to the enlargement of the pearlite colonies in the microstructure during the heat treatment process. Enlarging the pearlite colonies is a diffusion-driven process where carbon diffuses from the ferrite phase to form lamellar layers in the adjacent pearlite colonies. The average grain size for these samples was 44.3 μm with a standard deviation of 12.45.

The cross-section of the 900 HTBT substrates on the other hand had three regions that developed from the surface to the substrate's core during the treatment; an outer upper bainitic case, conventional bainite and pearlite regions underneath it and the core region. These phases developed due to preferential phase transformations in the various areas due to varying cooling rates across the cross-section of the substrates. The average grain size of these substrates was 23.13 ± 10.6 μm. The shrinking of the pearlite grains was due to the recrystallization of the ferrite grains at the grain boundaries as shown in Fig. 3(c). This is associated with the dissolution of the initial low temperature phases to form the gamma phase (austenite) at 900 °C. Precipitates of the ferrite phases begin to form in the grain boundaries of the austenitic grain boundaries before forming lamellar pearlites phase with the grains. Larger pearlite grains grow, as more time is allowed for diffusion above the recrystallization temperature of the steel. The grain boundaries of the bainite and pearlite regions in the case were not dominated by proeutectoid ferrite, as compared to the core region (Fig. 3(d and e)). The increase in carbon content due to the carbon defusion led to the formation of cementite at the grain boundaries, which is characteristic of hypoeutectoid transformtaitons.

The as-received 1045 steel substrate had an average grain size of 33.79 ± 11 μm, as shown in Fig. 3(g). The average lamellar spacing of the pearlite structure was 0.29 μm, as indicated in Fig. 3(f).

3.2. Hardness

The microhardness results for the substrates are shown in Fig. 3(h). The hardness of the material increased from 2.69 ± 0.33 GPa (untreated) to 2.75 ± 0.37 GPa (500 HTBT substrates) to 3.00 ± 0.062 GPa (900 HTBT substrates). The hardness of the biotreated substrates, therefore, increased as the treatment temperature increased from 500°C to 900°C. This was attributed to the case hardening effect that was observed in the 900 HTBT substrates, which was non-existent in the 500 HTBT substrates.

Fig. 3(i) shows the microhardness profile from the surface to the core of the 900 HTBT substrates. The hardness was taken from the surface to a 10 mm distance towards the core. The measured hardness was 3.00 ± 0.062 GPa at the surface, which dropped to 2.76 ± 0.056 GPa at 1 mm into the substrate and finally (averaged at about 1.14 ± 0.073 GPa from 2 mm to 10 mm at the core. This result was consistent with the case depth estimation from the SEM and optical microscopy images. This case hardening effect of a hard case and a relatively soft core is typical of carburizing case-hardened materials and is desirable for bearing, gears, and shaft applications.

It is worth noting here that the hardness and microstructural properties (from the case to the core of the microstructure) can be controlled for various applications by varying the cooling rate and heat treatment conditions. The hardness measurements taken across the cross-section of the 500 HTBT substrate (as shown in Fig. 3(i)) reveals a hardness of 2.75 ± 0.37 GPa at the surface, 2.6 ± 0.021 GPa at 1 mm below the surface,

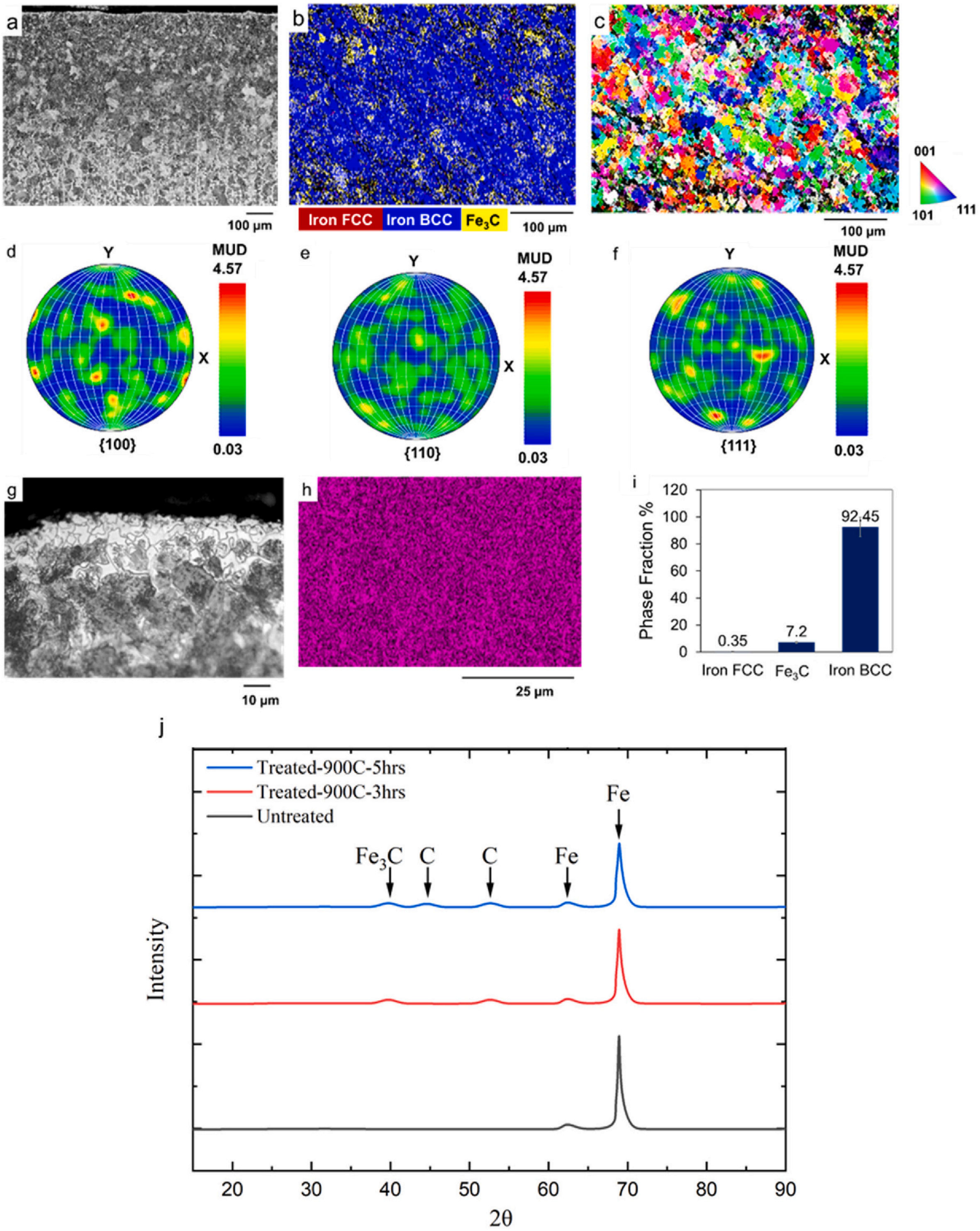

Fig. 4. EBSD, SEM, EDS and XRD analysis of the cross-sectional case depth of 900 HTBT substrates (a) optical micrograph of 900 HTBT, showing a cross-sectional depth of ~600 μm, (b) EBSD phase mapping of cross-sectional depth of the 900 HTBT substrate, showing red for iron FCC phase, blue for BCC phase and yellow for Fe$_3$C phase, (c) EBSD phase orientation mapping of the 900 HTBT substrate, showing red for {0 0 1}, green for {1 0 1} and blue {1 1 1} directions, (d)–(f) {1 0 0}, {1 1 0} and {1 1 1} polefigure showing texture of the microstructure of the 900 HTBT substrate, (g) Optical image of upper and conventional bainite case showing an upper case depth of 21 μm, (h) case depth EDS analyses showing diffusion of carbon to a depth of ~370 μm from the substrates' surface, (i) phase fraction results for the microstructure of the 900 HTBT substrate, from the EBSD analysis, (j) XRD results for the surface of the untreated and treated substrates.

and levels out at an average hardness of 2.59 ± 0.38 GPa after 2 mm from the surface. The As-received substrate had a consistent hardness profile from the surface to the core of the cross-section due to hot rolling and microstructural homogenization by the manufactural.

3.3. *Crystallographic and phase mapping of substrate microstructure*

The crystallographic and phase maps of the treated and as-received substrates are shown in Fig. 4. The depth across these three regions was 600 ± 45 μm, as shown in Fig. 4(a) as estimated from the evaluation

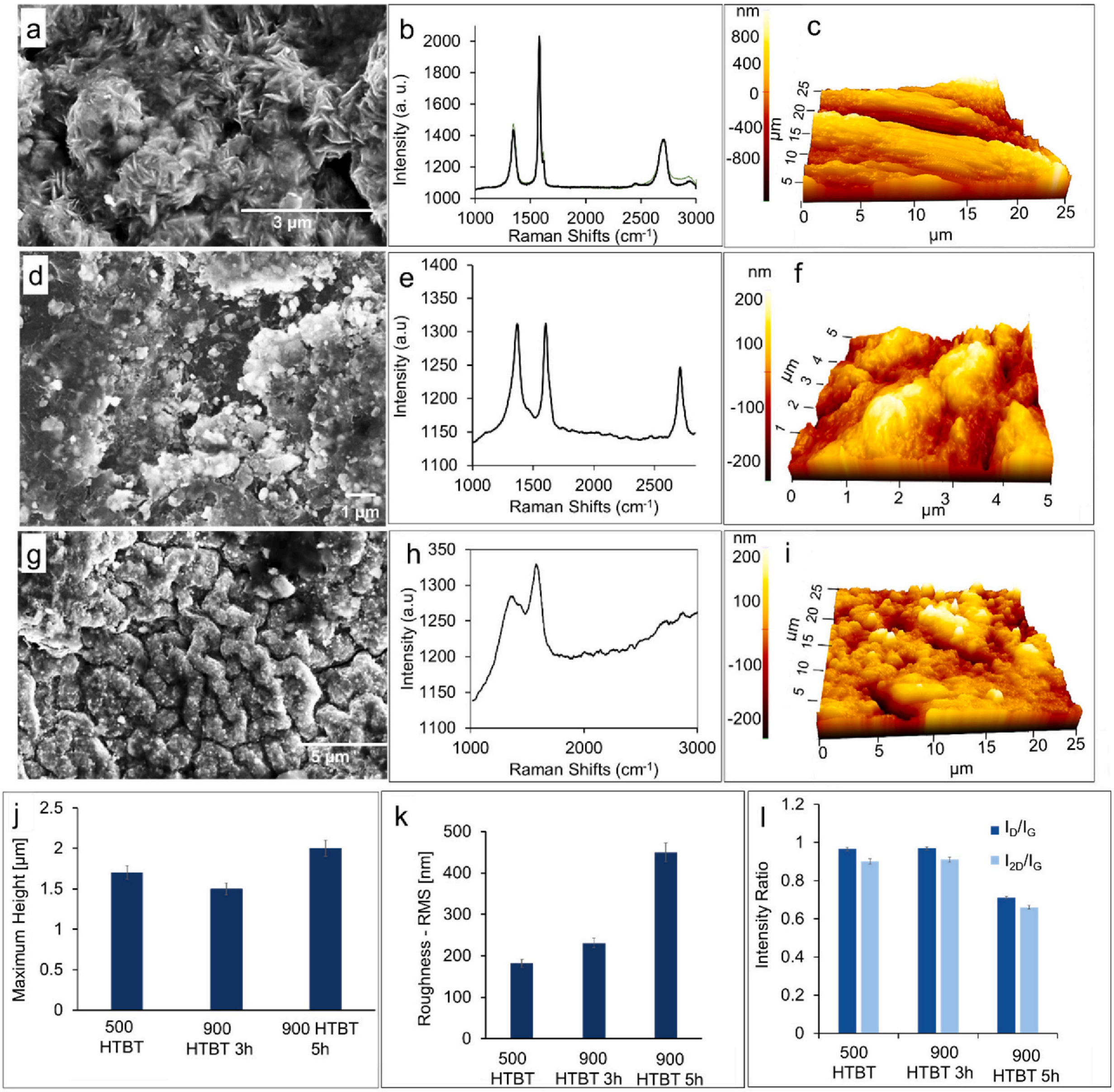

Fig. 5. Surface characterization of carbon coatings on substrates; (a) SEM results of the surface of the 5 h treated 900 HTBT substrates showing top layer carbon nanotube mesh, (b) Raman spectra of carbon structures on 5 h treated 900 HTBT substrate, (c) AFM topographical analyses of 5 h treated 900 HTBT substrate, (d) SEM image of the surface of the 3 h treated 900 HTBT substrates showing platelet deposits, (e) Raman spectra of deposits on 3 h treated 900 HTBT substrate, (f) AFM topographical analyses of 3 h treated 900 HTBT substrate, (g) SEM image of the surface of the 500 HTBT substrates showing carbon nano crystal precipitates and ridges. (h) Raman spectra of carbon deposits on 500 HTBT substrate, (i) AFM topographical analyses of 500 HTBT substrate, (j) AFM results of maximum coating height of the carbon variants on substrates, (k) AFM results of root mean square values of the surface of the biotreated substrates. (l) Plot of I_D/I_G and I_{2D}/I_G ratios for the Raman spectra of the various carbon coatings.

of the optical and scanning electron microscopy images. The upper bainitic case had a length of 21 ± 11 µm (Fig. 4(g) and the length of the bainite is 578 ± 26 µm, (Fig. 4a). These substrates' carbon diffusion depth was estimated as 370 ± 19 µm (Fig. 4(h). The average grain size across the three regions was 23.125 µm with a standard deviation 10.6. The phase mapping of the microstructure (Fig. 4(b)) reveals a dominant iron BCC – ferrite phase with intermittent Fe_3C – cementite phases in the microstructure. The cementite phases were more at the top layer of the case depth which supports the high hardness values observed in the hardness profile of the cross-section.

Fig. 4(c) is an EBSD crystallographic orientation image of the microstructure with red representing {0 0 1} direction, blue for {1 1 1} direction and green for {1 0 1} direction. This result reveals randomly the orientation of the grains in the microstructure in the {0 0 1}, {1 1 1} and {1 0 1} directions.

Fig. 4(d–f) presents a polefigure texture results for the case of the 900 treated substrates. The substrate had a heterogeneously textured microstructure made up of randomly textured ferrite phases in the {1 0 0} and {1 1 1} crystallographic direction (Fig. 4(d and f)). The polefigure for {1 1 0} crystallographic orientation relatively showed a homogeneous texture in the microstructure as shown in Fig. 4(e). The texture of a steel's microstructure influences the wear and hardness properties [39]. The grain size distribution and the heterogeneous textured microstructure that emanates from the presence of ferrites, pearlites and bainites [44]. In some cases, the distribution of inclusions also affects the texture of the steel as well. This affects the resistance of the material to deformation and wear under tribological conditions [40]. Heterogeneous textured structure with fine grains and fine bainite

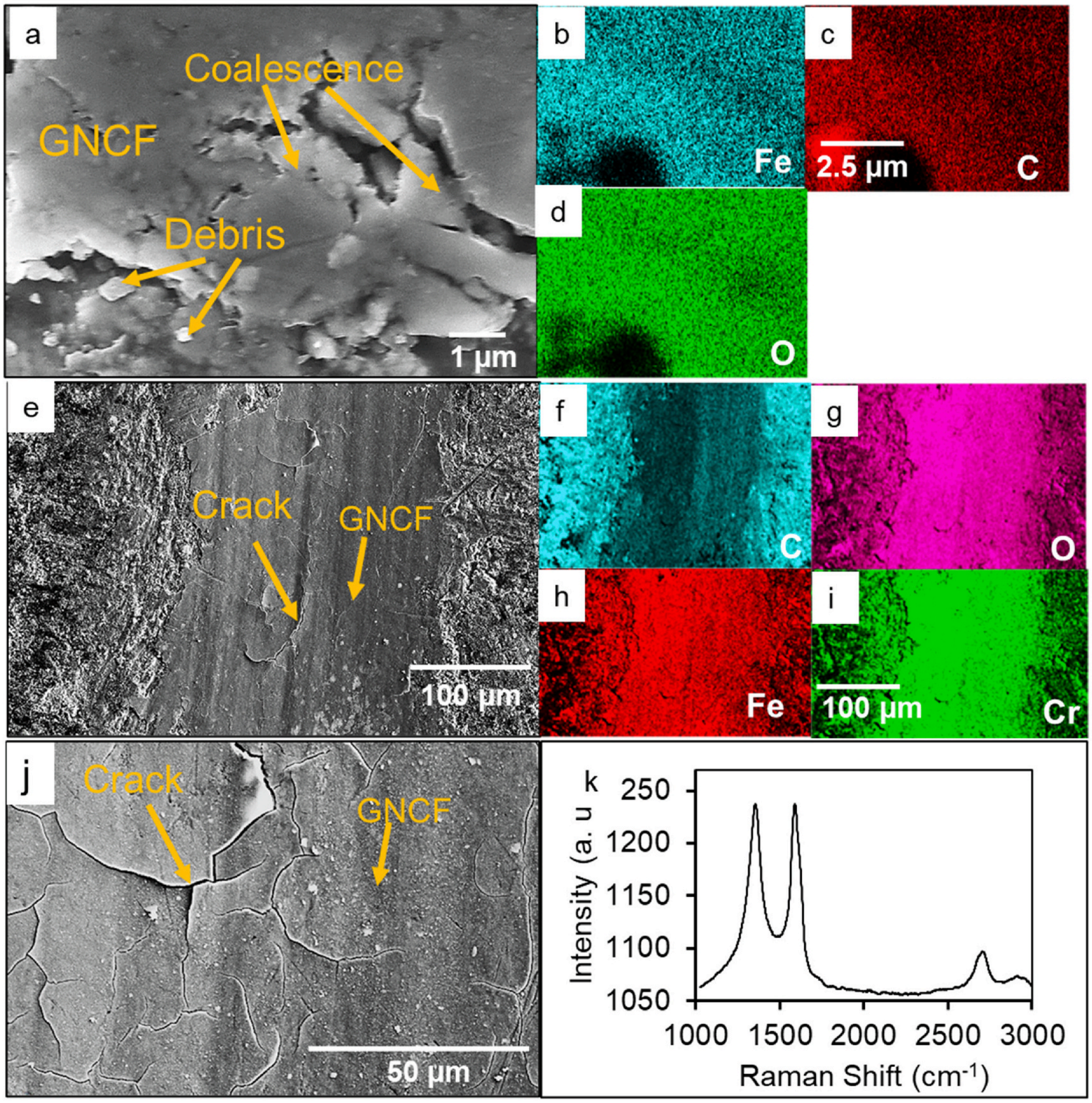

Fig. 6. SEM, EDS and Raman Scattering analysis of 30 min wear tracks of 3 h and 5 h 900 HTBT substrates (a) SEM micrographs of the 3 h wear tracks of the substrates after 3 min of wear test showing graphene nanocomposite film formation, (b)–(d) EDS results of 30 min wear tracks of 3 h HTBT substrate showing C, Fe and O, respectively, (e) SEM image of 30 min wear track on 5 h treated substrates showing graphene nano composite film covering wear tracks, (f)–(i) EDS results of wear tracks showing C, O, Fe and Cr, respectively, (j) high magnification SEM image of wear tracks on 5 h treated substrates showing graphene nanocomposite film with cracks (k) Raman spectrum for graphene oxide on wear tracks, indicating tribo-oxidation after 30mins of wear.

structures as observed in the 900 HTBT substrates (Fig. 4(a–f)) often leads to improved hardness and wear resistance [41].

Heat treatment temperature and substrate carbon concentration both affect case hardening. A cross-sectional micrograph of 900 HTBT substrates (Fig. 4(g)) shows distinct microstructures in the case versus the underlying region. Qualitative EDS results (Fig. 4(h)) indicate high carbon concentrations at grain boundaries, inhibiting dislocation movement and increasing hardness.

From Fig. 4(i), the phase fractions are 0.35 ± 0.025 % FCC iron (retained austenite), 92.45 ± 7.15 % BCC ferrite (proeutectoid ferrite), and 7.2 ± 0.5 % cementite (Fe_3C), aligning with optical and SEM observations. The XRD data (Fig. 4(j)) confirm dominant BCC ferrite and some cementite. The absence of characteristic carbon peaks at 44° and 53°, along with the missing Fe_3C peak at 40° (compared to the as-received condition), verifies carbon diffusion into the substrate and the formation of cementite in the treated samples.

The spectra of the 900 HTBT substates heat treated for 3 h revealed Fe_3C peaks at 40° and a carbon peak at 53° (Fig. 4(j)). This carbon peak is characteristic of graphene platelets and consistent with prior works [42,43]. This was also confirmed with the SEM image and Raman results in Fig. 5(d and e). The spectra for the 900 HTBT 5 h substrates showed graphene peaks at 44° (1 0 0) and 53° (0 0 4) [44–46]. The appearance of the 44° peak indicates an increase in the crystallinity of the graphene structure as the treatment time is increased [44]. These peaks are also indicative of the presence of multiwalled carbon nanotubes [47,48] as observed in the SEM and Raman results in Fig. 5(a and b).

3.4. Characterization of samples

The FTIR results of the Manihot esculenta biowaste powder before the treatment is shown in Fig. 1(b). The spectrum shows peaks at 1038 cm^{-1}, 1244 cm^{-1}, 1606 cm^{-1} and 1654 cm^{-1}, which represents CO (carboxylic), CH, NO (Nitro) and NH functional groups in the biowaste powder [49]. The bands at 2132 cm^{-1} and 2326 cm^{-1} were attributed to CN and $C\equiv N$ (nitrile or cyanyl) stretching [50]. Also, the peaks at 2927 cm^{-1}, 3285 cm^{-1} and 3656 cm^{-1} represents CH, OH and N-H functional groups. The high temperature treatment of the biowaste powder breaks the bonds and vaporises most of these compounds leaving behind a

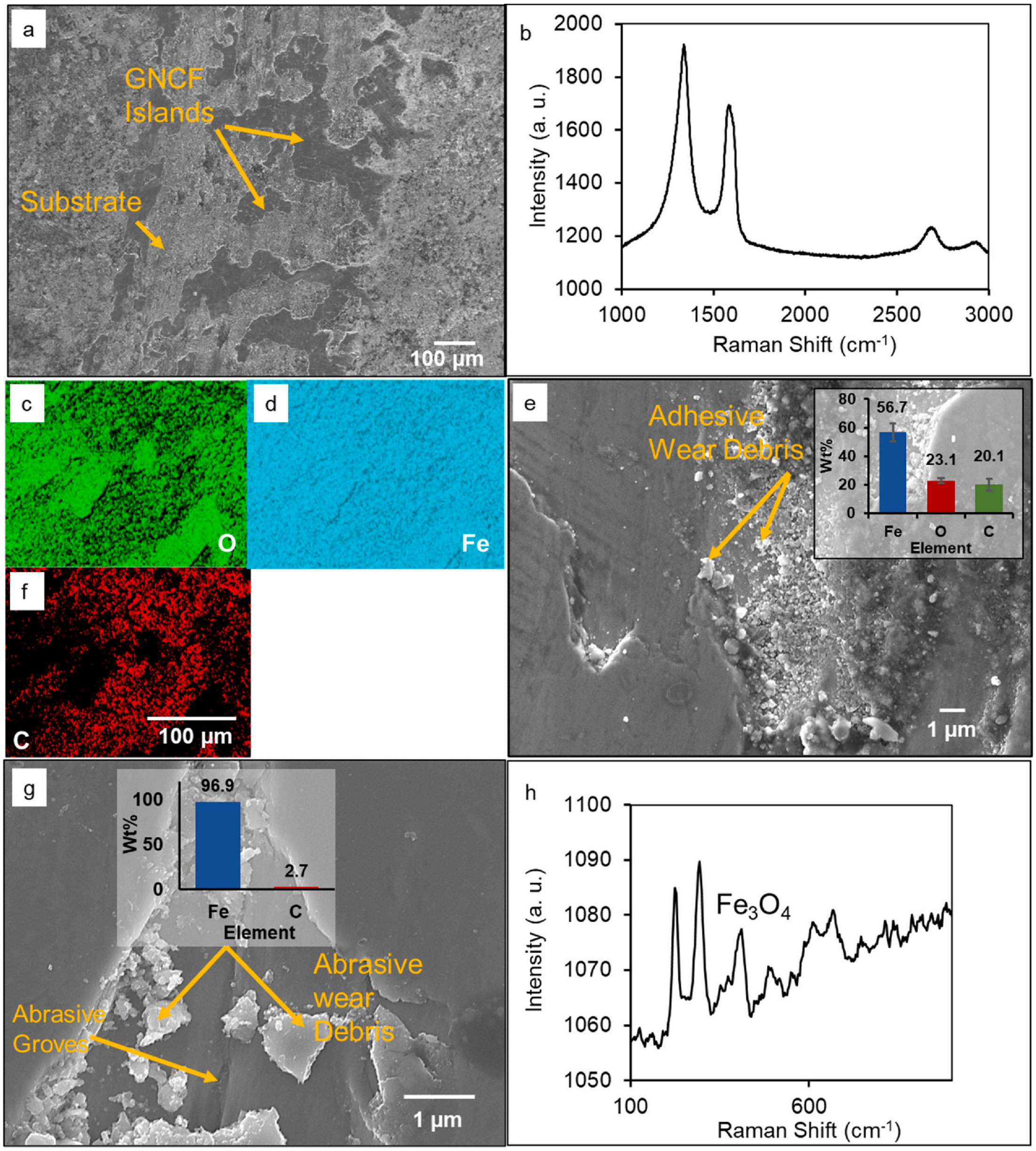

Fig. 7. SEM, EDS and Raman Scattering analysis of 90 min and 180 min tracks of 900 HTBT substrates; (a) SEM micrographs of 90 min wear track of substrate, showing graphene nanocomposite film islands (b) Raman microscopy results of 90 min wear tracks showing stress – thermo induced graphene nano-structures, (c)–(f) EDS results of wear tracks showing O, Fe and C, respectively, (e)–(g) SEM image and EDS results of wear tracks of 3 h and 5 h 900 HTBT substrates, respectively, after 3 h of wear, showing adhesion wear and abrasion wear between the ball and the substrates with iron oxide debris. (iv) Raman spectra of debris on wear tracks of samples after 3 h of wear test, showing bands of Fe_3O_4 as adhesion wear products.

concentrated carbon powder as shown in prior work [49]. This then creates the rich conditions that facilitates carbon diffusion and crystallization.

Fig. 5(a) is an SEM image of the surface of the 5 h treated 900 HTBT substrates, which reveals irregular multiwall carbon nanotube mesh deposition with patches, with nanotubes of diameter 30 ± 10 nm. The EDS analysis of these substrates showed qualitatively high carbon content on the substrates. The Raman spectroscopy show results for defective graphene multi-wall, that have D peaks at 1346 cm^{-1}. The D peak is acquired from the disordered vibrations of the graphene structure and the degree of distortion which characterizes the defective graphene structure [26,51–53]. The lowest D peak distortion, which represents less defective graphene structures, was observed on these substrates. The G bands of the Raman spectra for this specimen were at 1577 cm^{-1}. This peak emanates from the stretching vibration of the sp^2 carbon atomic pair forming the graphene [51]. The 2D bands of the Raman spectra on these samples were at 2716 cm^{-1}, as shown in Fig. 5(b). This peak is obtained from the inelastic scattering of biphotons from the graphene layers [53,54]. The shape and height of this peak provide useful information about the number of layers in the graphene structure. A sharp rise and fall conical tip represent few graphene layers, while the domed shape represents amorphous carbon structures [53–55]. The mean I_D/I_G ratio of the spectra was 0.72 (Fig. 5(I)), which represents graphene with multi-wall structure and corresponds to Raman footprints for graphene deposited with solution-processing [16] on steel substrates. It also affirms the degree of defectiveness in the graphene structure. The I_{2D}/I_G ratio was also determined to be 0.66, this is an essential feature in distinguishing few-layer graphene structures from multiple-layer carbon structures in graphite [55].

The SEM images of the 3 h treated 900 HTBT substrates (Fig. 5(d))

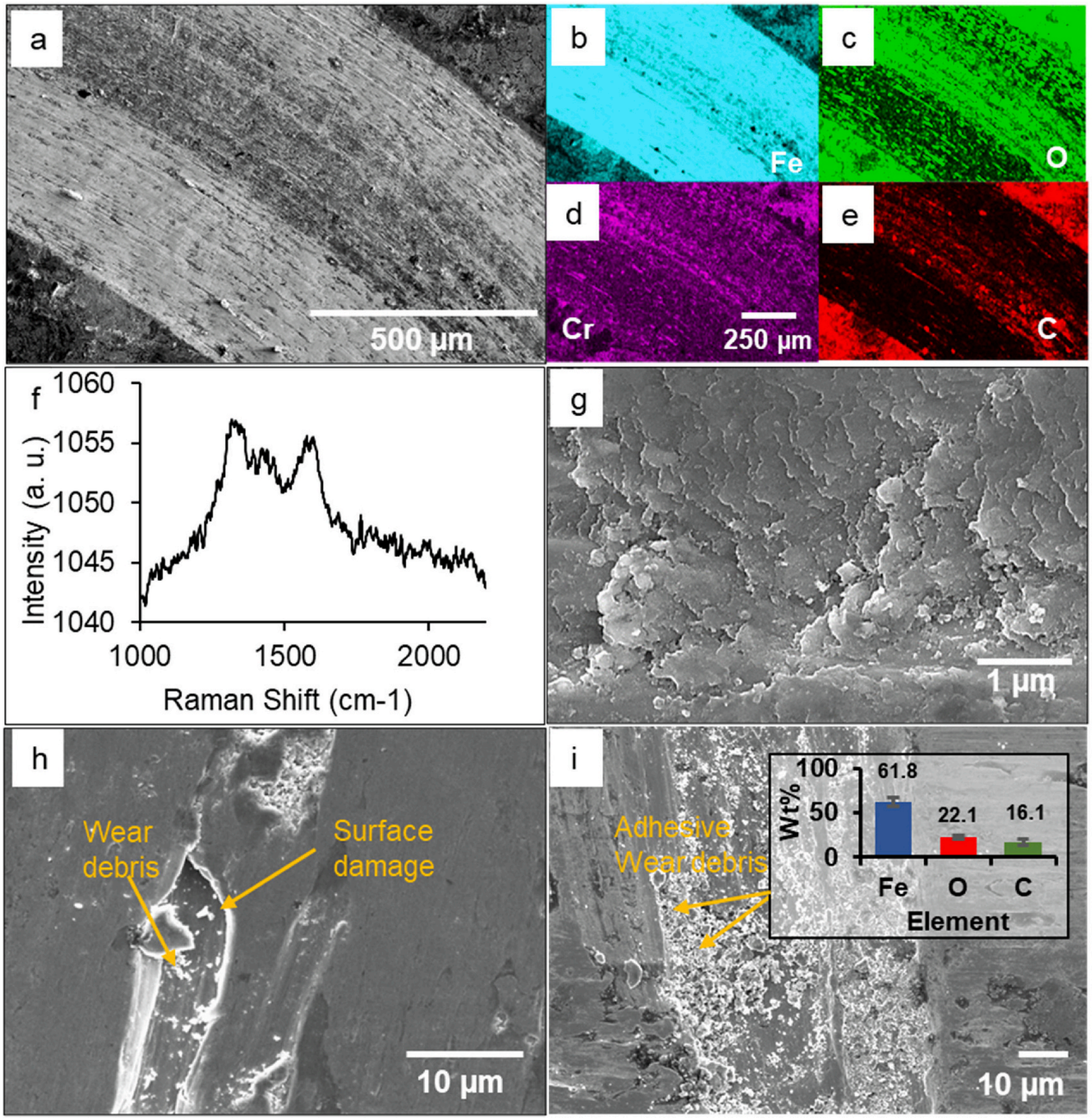

Fig. 8. SEM images, EDS, Raman spectra and Optical of 500 HTBT and As-received substrates (a) SEM micrographs of 500 HTBT substrate wear tracks after 30 min of wear, showing micro groves on the substrate, (b)–(e) EDS maps of 30 min tracks of 500 HTBT showing Fe, O, Cr and C distribution in it, (f) Raman results of 30 min track of 500 HTBT, revealing the presence of amorphous graphite on the wear tracks. (g) 90 min wear track of 500 HTBT substrates showing adhesive wear, (h) 180 min wear track of the untreated substrates showing abrasive wear, (i) SEM image and EDS results of 30 min track on untreated substrates, showing adhesion wear debris.

reveal the deposition of graphene platelets with patches on the surface of the substrates. The AFM image in Fig. 5(f) also shows ridges with maximum height of 1.5 ± 0.08 µm (Fig. 5(j)) and a root mean square roughness value of 231.3 ± 10.4 nm (Fig. 5(k)). The Raman spectra for these coatings had G peaks at 1588.19 cm^{-1}, D peaks at 1351.45 cm^{-1} and 2D peaks at 2703.55 cm^{-1}. The intensity ratio (I_D/I_G) for this spectrum was 0.97 (Fig. 5(I)). This shows that the graphene structure in this coating is more defective than that for the 5 h treated 900 HTBT substrates discussed above. Increasing the deposition temperature, therefore, leads to less defective graphene structures. The intensity ratio (I_{2D}/I_G) ratio was 0.91, higher than that for the 5 h 900 HTBT substrates. This is an indication of higher number of carbon sheets in the graphene multilayer platelets in the 3 h 900 HTBT substrates than in the 5 h 900 HTBT substrates.

The Raman spectra for the 500 HTBT substrates revealed graphene nanocrystal deposits on the surface of the substrates with D peaks at 1357 cm^{-1}, G peaks at 1565 cm^{-1} and 2D peaks at 2720 cm^{-1} as shown in Fig. 5(h). The I_{2D}/I_G and I_D/I_G ratios were 0.97 and 0.9, respectively. The D bands of the Raman spectra for these samples had a broader shape, which shows a more defective graphene structure than those for the other treated conditions.

3.5. Wear

3.5.1. Wear behavior of treated and untreated substrates

Wear experiments were conducted on the treated and untreated substrates. The SEM image in Fig. 6(a) reveals the early formation (up to ~3 min of wear) of graphene composite films in the wear tracks of the 900 HTBT substrates. The EDS results in Fig. 6(b–d) show O, C, and Fe in the tracks. The graphene composite film was fully developed to cover the wear tracks after testing for 30 min as shown in Fig. 6(e and j). This led to reduced wear rates and protection from adhesive and abrasive wear mechanisms on the substrates treated at 900 °C.

The characterization of the wear tracks of the 3 h and 5 h 900 HTBT substrates (with Raman spectroscopy within 30 min intervals) revealed D and G graphene peaks (that were taken initially) were distorted, with a different I_D/I_G ratio of 0.98 (Fig. 6(k)). The bands reveal defective and amorphous structures which suggests graphene oxide (GO) presence.

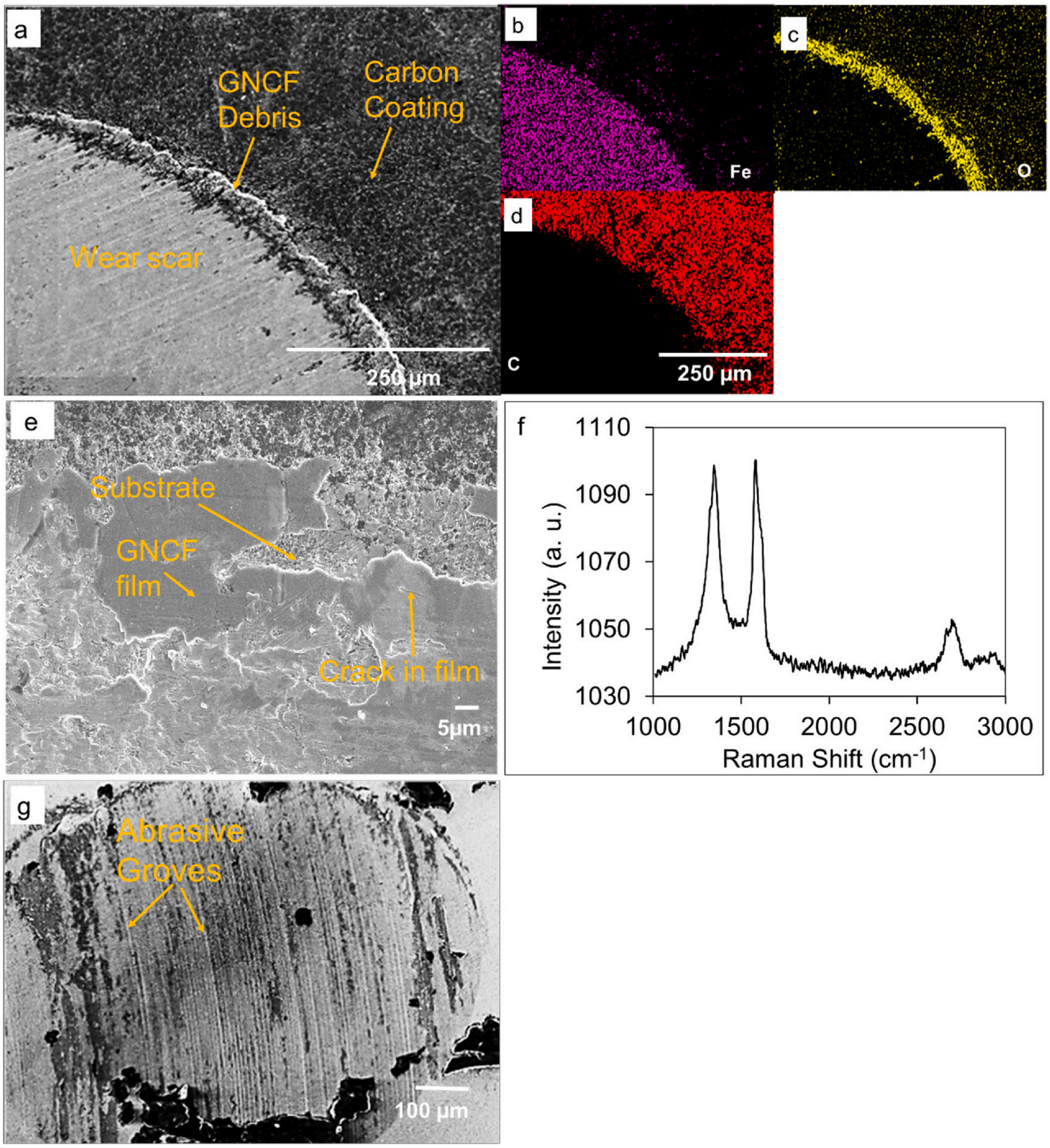

Fig. 9. SEM images Raman spectrum, EDS, wear rate and wear merit index analysis of ball scar and substrates, (a) SEM image of 3 h 900 HTBT treated ball scar after 30 min of wear, showing pile-ups at the edges(b)–(d) EDS results of 3 h 900 HTBT treated ball scar after 30 min wear showing Fe, O and C distributes in the tracks, (e) SEM image of GNCF on the treated ball after 1000 cycles of wear, (f) the Raman spectrum for GNCF in film, indicating tribological – oxidation after 1000 cycles of wear (g) SEM image of untreated 100Cr steel ball scar.

The D peaks of the spectra were at 1344 cm^{-1}, the G peaks were at 1605 cm^{-1} and the 2D peaks were at 2693 cm^{-1}. The results from the EDS show a high concentration of oxygen (37.6 wt%) and carbon (14 %) in the wear tracks (Fig. 6(f–i), affirming the presence of GO. The SEM micrographs taken from the wear tracks in Fig. 6(a) also revealed debris with analogous concentrations of C, Fe, and O (Fig. 6(b–d). This indicates tribological – oxidation phenomena in the wear tracks. Tribological oxidation occurs when ambient oxygen is supplied to the point of contact between the counter body and the graphene layer as the local temperature rises during the sliding action. This is facilitated by high friction and the heat produced during the mating interactions that cause the oxygen molecules in the immediate environment to easily react with the graphene lattice [11]. This leads to the formation of oxygen-containing functional groups such as hydroxyl, epoxide and carbonyl [56]. The functional groups embers in the surface of the graphene sheets and lead to the gradual degradation of its structure. The bonds of the graphene are then weakened leading to the potential exfoliation of the carbon sheets. This process then yields defects or edge pining effects that act as active sites for impending oxidation action [57].

The measured temperature under the ball with the infrared camera was 28 ± 0.3 °C. It was noticed that the temperature was high under the ball but dissipated quickly into the material. The Raman spectroscopy results show few spectra with features as revealed in Fig. 7(b) in the tracks, but the graphene oxide spectra are the mostly predominant. Therefore, a GO and nanocrystal graphene films are formed between the substrate material and the counter body, thereby decreasing abrasive and adhesion wear [11]. This resulted in the modification of the wear mechanism of the substrates.

Islands of graphene nanocomposite films were observed in the SEM images of the wear tracks of the 900 HTBT substrates after 90 min of the test (Fig. 7(a)). These were formed by removing the graphene composite films from the wear tracks due to the continuous interaction of the mating surfaces. Fig. 7(b) shows the Raman results for the 90 min wear tracks for these substrates. The spectrum shows modifications in the

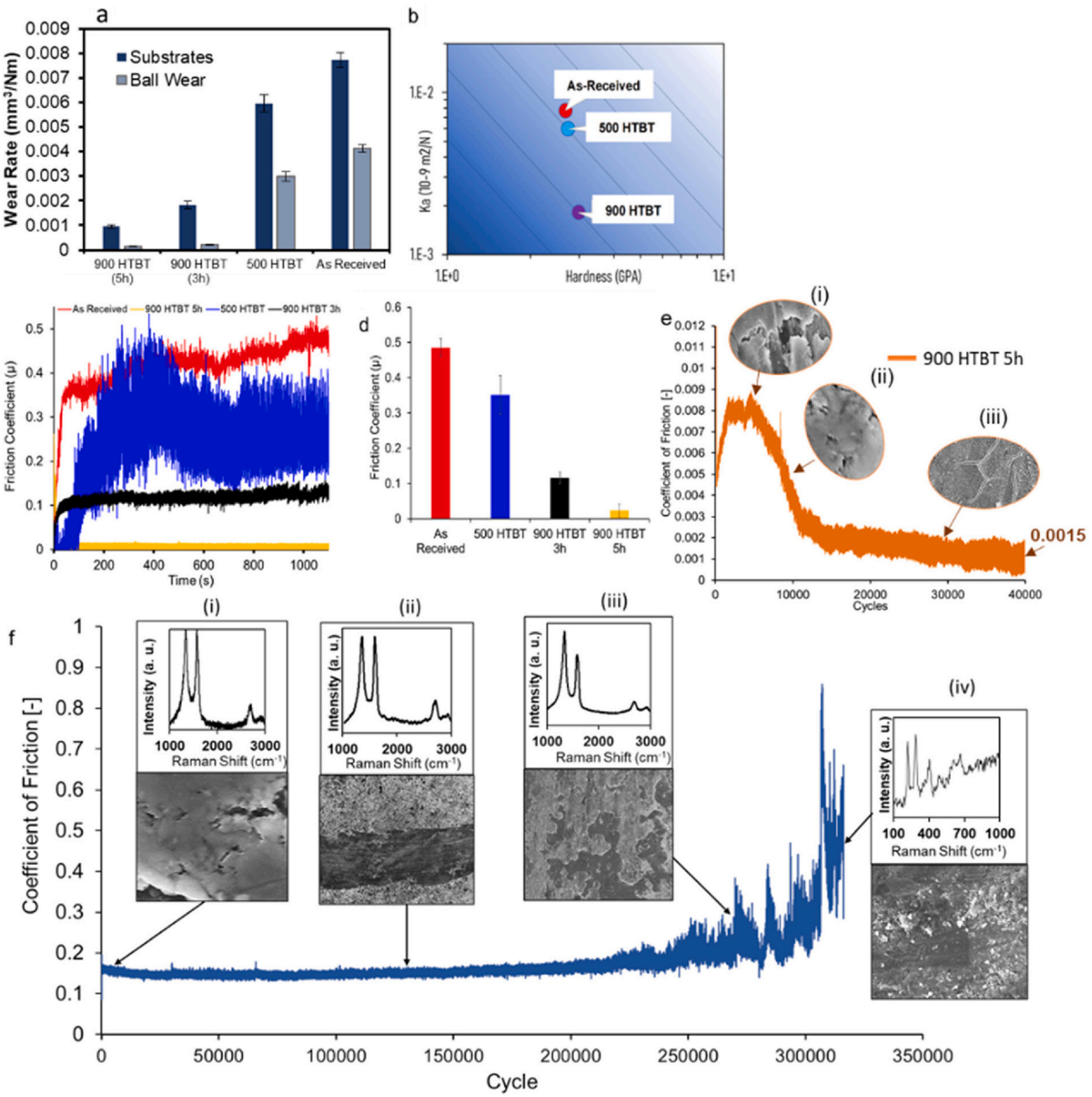

Fig. 10. Friction, Raman Spectroscopy, wear rate, wear merit index and SEM wear results of substrates; (a) Wear rate results for treated and untreated balls and substrates, and (b) wear merit index for the treatments showing improved wear performance of the treated substrates as the treated time and temperature increases. (c) friction coefficient versus time (s) plot for treated and untreated samples, (d) CoF results for the untreated and treated samples showing the reduction in CoF values as the temperature and time of treatment is increased, (e) superlubricity plot of coefficient of friction versus cycles for 900 HTBT 5 h treated substate (i)–(iii) SEM images showing the film state of development at different regimes, (f) friction coefficient evolution and wear stages of 3 h treated 900 HTBT substrates, (i)–(iv) Raman spectra and SEM wear images of wear tracks showing the stages of wear of the treated substrates.

carbon peaks compared to the dominant GO bands observed earlier. The D peak was positioned at 1344 cm^{-1} and the G peak was at 1578 cm^{-1}. The intensity ratio (I_D/I_G) for the peaks was changed to 1.14, a footprint of graphene nanocrystals, and carbon nanotubes. These results have also been observed on wear tracks of graphene-like surfaces [16,18]. The products identified are evidence of stress and thermo-induced processes that cause structural variance in graphene. These processes happen due to the extreme wear action under the counter body. The process is typically known as stress induced graphitization [58].

The graphene nanocrystals embedded in the wear tracks combine with the graphene composite thin films to form a layer that intercalates the wear tracks and the counter body. Abrasive and adhesion wear mechanisms are minimized as the contact interactions between the counter body and substrate is reduced. Furthermore, the graphene nanocrystal bands dominated the Raman results for these wear tracks, traces of GO spectra as shown in Fig. 6(k) were noticed in the wear debris. The EDS analyses (Fig. 7(c–f)) for these tracks indicate ~14.6 wt% Carbon and ~36.7 wt% oxygen. Also, the EDS results reveal an Fe weight percent of ~49.8 wt%, from the substrate and counter body materials.

The SEM image in Fig. 7(e–g) shows wear debris on the substrates after wearing for 180 munities. The Raman spectra of the debris as shown in Fig. 7(h) reveal bands of Fe_3O_4 on the wear tracks. The EDS results in Fig. 7(e) also show Fe weight percent of 56.7.8 ± 6.13 wt, O weight percent of 23.07 ± 1.85 wt% and C weight percent of ~20.07 ± 4.28 wt%. These tribological oxidation products of Fe and O are formed and detached from the wear tracks. This indicates adhesion wear mechanism as the graphene composite film is broken through and eroded beyond 90 min of the test, marking the completion of the graphene protection. Fig. 7(g) shows an SEM image and EDS results of wear tracks of 5 h 900 HTBT after 3 h of wear, showing abrasion wear between the ball and the substrates. The EDS results of these debris did not have oxides in them as seen in the debris of the adhesive wear products. A summary of the wear stages of these samples is shown in the schematic in Fig. 12(a–d).

The wear of the 500 HTBT substrates exhibited adhesion wear after the 30-munite wear test as shown in Fig. 8(a) with its corresponding EDS results in Fig. 8(b–e). The Raman spectrum in Fig. 8(f) for the wear track showed a deformation in the peaks obtained for the treated 500 HTBT substrates, with an I_D/I_G ratio of 1.00. This shows traces of amorphous graphene oxide in the wear tracks. The wear tracks in Fig. 8(g) (taken after 90 munities of test) reveal layer-by-layer removal of material due to adhesion wear. The surface also shows micro groves formed due to abrasive action. There were few wear debris in the tracks.

The untreated substrates' wear tracks after 30 min of wear test also show adhesive interactions between the steel ball surface and that of the substrate (Fig. 8(i). After 180 min during the test, the tracks showed microcracked with material pull-outs on the surfaces, revealing abrasive wear mechanism (Fig. 8(h)). The wear mechanisms accountable for wear in the 500 HTBT and untreated substrates were predominantly adhesive wear with traces of abrasion wear. Contrary to the mechanism noticed on the 900 HTBT substrates, affirming the impact of the graphene protection on those substrates.

3.5.2. *Counter body wear*

Fig. 9 presents the SEM micrographs of treated and untreated ball scars. Fig. 9(a) shows graphene nanocomposite film debris around the peripheral of the scar on the 3 h 900 HTBT-treated balls used on the 3 h 900 HTBT-treated substrates. The EDS analysis of the treated 100Cr steel balls in Fig. 9(b–d) shows the pile up to contain a high O, C and Fe concentration, affirming the presence of GO and iron oxide. These tribo-oxidation products are formed in the track to induce low friction and pushed to the peripheral of the wear scar due to rotational motion.

Fig. 9(e) shows the graphene nanocomposite films formed on the ball wear scar after 1000 cycles of wear. The SEM micrograph shows patches and cracks in the film as observed on the wear tracks of the substrates. This reveals a film-on-film mechanism for the superlubricious conditions. Graphite film transfer on counter bodies has been identified as a favourable condition for ultra-low friction [59]. In this mechanism, the carbon sheets slide over each other easily due to the weak Van der Waals forces between them [11,60]. The average friction force for the sliding motion is, therefore, reduced. The film is likely to be remove quickly after formation due to the rotational motion [61,62]. The stability of the film in the wear tracks of the substrate and on the counter body is crucial to sustain superlubricity [62]. This phenomenon is observed in this work as shown in Fig. 10.

The surface of the untreated ball scar shows micro groves with debris at the edges Fig. 9(a). The wear surface did not show significant abrasive wear, which strongly indicates the dominance of adhesive wear.

3.5.3. *Wear merit indices and wear rates of treated and untreated substrates*

The wear rates of the as-received substrate material (Fig. 10(a)) is 0.00773 ± 0.0003 mm^3/Nm. Upon treatment, the 500 HTBT samples had wear rate of 0.00596 ± 0.0004 mm^3/Nm, whereas that of the 3 h and 5 h 900 HTBT substrates were 0.00182 for ±0.0002 mm^3/Nm and 0.00095 ± 0.00008 mm^3/Nm. Thus, a wear rate reduction of 88 % for the 5 h 900 HTBT substrates, 76 % for the 3 h 900 HTBT and 15 % for the treated 3 h 500 HTBT substrates as compared to the untreated substrates. An important and remarkable decrease in wear rates were achieved by the new high temperature biowaste method at 900 °C. This is due to the existence of GO and nanocrystals films between the substrates and counter body, which were confirmed by the Raman spectra and SEM images. Therefore, abrasive and adhesive wear due to iron oxide interactions (as seen in the wear tracks of the as-received material) were prevented in the biotreated substrates' wear. This led to the observed significant decrease in the wear rates. The wear rates are, however, higher than some diamond-like coatings which have wear rates of 5.07 $\times 10^{-7}$ mm^3/Nm and CoF of 0.8 in dry N_2 and 4.94 $\times 10^{-8}$ mm^3/Nm with CoF of 0.17 for humid air [16]. Composite coatings of graphene on Ni have comparable wear rates of 8.6 $\times 10^{-4}$ mm^3/Nm with CoF of 0.1 [63]. Graphene/$MoWS_4$ composites also have wear rates of 1.6 $\times 10^{-6}$ mm^3/Nm with a CoF value of 0.008 [64]. As observed in this work, the treatment temperature and time influence the CoF and wear rate values. This can be explored to achieve even lower wear rate.

The wear rates of the counter body as shown in Fig. 10(a) reveals the trend noticed for the various substrates. The wear rates of the treated and untreated 100Cr steel ball were 0.004128 ± 0.000165 mm^3/Nm for the As-received 1045 steel, 0.002996 ± 0.000139 mm^3/Nm for the 500 HTBT substrates, 0.000199 ± 0.0000139 mm^3/Nm for the 3 h 900 HTBT substrates and 0.000132 ± 0.0000105 mm^3/Nm for the 5 h treated 900 HTBT. This implies a wear rate reduction of 96 % for the 5 h 900 HTBT substrates, 95 % for the 3 h 900 HTBT substrates and 27 % for the treated 500 TBT substrates as contrasted with that of the untreated substrates. These decrease in wear rates were also associated with the graphene protection as solid lubricant [26–30].

The plot of the wear rates of the substrates versus their hardness predicts the wear merit index of the materials. It is a parameter for material selection for wear applications. Fig. 10(b) was done to assess the level of enhancement in the wear properties of the 1045 steel concerning the HTBT method. The 500 HTBT substrates were identified to have inferior wear KaH values than those for the 900 HTBT substrates. This shows an enhancement in the performance index of the treated substrates compared to the untreated ones.

The wear of the untreated materials was, therefore, characterized by high wear rates with adhesive and abrasive wear. The wear mechanisms on the 3 h and 5 h treated 900 HTBT substrates were similar. Both had nanocomposite films made of graphene variants formed in their wear tracks. The Raman results of the wear tracks also show the presence of modified carbon structure with an intensity ratio (ID/IG) of 1.14 (Fig. 7b), which is a footprint of carbon nanotubes. These Raman results are different from those for graphite, which is a carbon structure with many carbon layers. The wear rates of the 900 HTBT substrates was low until the graphene nanocomposite films were removed from the wear tracks (Fig. 10a). The wear life of the 500 HTBT samples was high (as contrasted to the 900 HTBT samples) and did not have graphitic protection (Fig. 10a). The Raman spectra of the wear tracks reveal distortions in the carbon structures due to tribo-catalysis/tribo-oxidation to form graphene oxide (with a different I_D/I_G ratio of 0.98) as part of the film (Fig. 9f). This film was, therefore, called graphene nanocomposite film (GNCF).

3.6. *Friction behaviour and analyses*

The average CoF of the 900HTBT that was treated for 3 h was 0.11 ± 0.015 and that of the substrates treated for 5 h was 0.023 ± 0.017. The average CoF value of the 500HTBT samples was 0.34 ± 0.064 and that of the as-received substrates was 0.48 ± 0.19 (Fig. 10(c and d)). This shows that the graphene coating decreased the CoF value of the as-received steel by 95.20 % for the 5 h 900HTBT substrates, 77.08 % for the 900 HTBT substrates treated for 3 h, and 29.17 % for the 500 HTBT substrates that were treated for 3 h. This suggests the capability of employing these coatings for solid lubrication setups. There were notable fluctuations in the friction curve of the 500 HTBT substrates due to a pronounced stick-and-slip mechanism, influenced by surface roughness, limited lubrication, and sliding velocity [65]. The lowest portions of the curve correspond to sticking conditions, the positive slope indicates creeping, and the negative slope signifies sliding [65].

A superlubricious CoF value of ~0.0015 was observed in this work for the substrates treated at 900 °C for 5 h (Fig. 10(e)). The

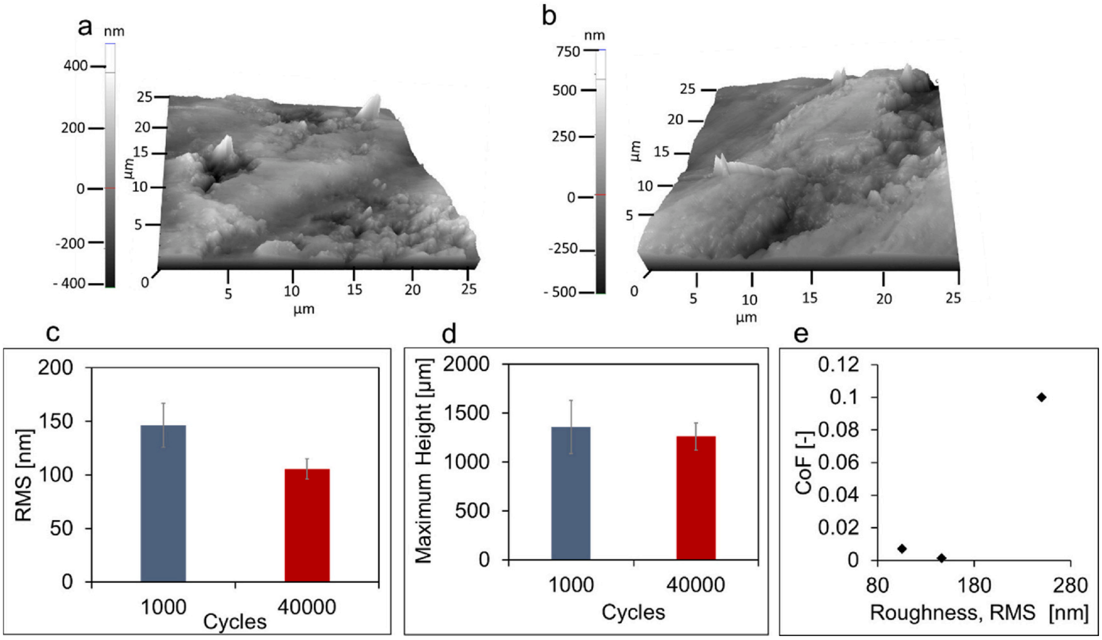

Fig. 11. AFM analysis of multiple nano- micro-contact interactions of the superlubricious wear tracks; (a) AFM image of 40,000 cycles superlubricious wear track of the 900 HTBT wear (b) AFM image of 1000 cycles superlubricious wear track of the 900 HTBT wear, (c) Root mean square roughness versus number of cycles plot for the superlubricious wear tracks, (d) maximum height on the coatings versus number of cycles plot for the superlubricious wear tracks, (e) Coefficient of friction corelation with root mean square roughness values of the 900 HTBT superlubricious wear tracks.

superlubricious results shown in Fig. 10(e) shows an initial low CoF value less than 0.004, which represents the interaction between the graphene-like coatings, on ball and substrate, at the early stages of the film formation. The curve then plunges to a maximum average CoF value of 0.0079 ± 0009. The SEM micrograph of this regime (Fig. 10(ei)) shows the formation of graphitic flakes in the wear tracks that are normally associated with edge pinning and pulling, phenomena that leads to increase in the CoF values [66,67]. The CoF value then drops after this process, as the nano flakes coalesce (Fig. 10(eii) to form the graphene nano composite films that cover most parts of the tracks. Fig. 10(eiii) shows the SEM micrograph of the stabilized regime which reveals cracks in the graphene nano composite film. The CoF value subsequently averages at 0.0015 ± 0.00085 at ~40000 cycles before the loss of superlubricity.

The macroscale superlubricity observed in this study was associated with the existence of multi-layered carbon nanotubes and crystals inducing multiple microcontact points in the tracks on the 900 HTBT substrates. This is also inspired by tribocatalysis in the tracks [68]. The stress conditions and temperature in between the counter body and the substrate induced tribological oxidation and graphitization of the carbon structure. These led to the formation of GO and graphene nanocrystals, as shown in the Raman results. The formed composite films on counter body and substrates, with cracks in them, interacted at the submicron levels to decrease largely the CoF values of the treated substrates. The graphene nanocrystals also serve as nano rollers which enhance frictionless sliding, as observed in prior work [18]. The sliding contributions of these constituents of the graphene composite films and the multi-layered nanotubes lead to the ultralow friction levels that were observed.

Ultralow friction induced by carbon films and nanocrystals are also attributed to two mechanisms, which are, interactions of weak interlayer Van der Waals bonds and incommensurability [17,60]. To attain ultra-low friction, the mating surfaces are expected to be incommensurate. Thus, there is a mismatch between the mating layers such that they slide pass each other with no energetically preferred positions and with little energy loss [69]. The graphene nanocrystal shells are considered to be rolled up carbon layers having chiral index (n, m). The independence of the (n, m) indices results to the incommensurable conditions on the nanocrystal shells. Furthermore, commensurability is attained only under conditions where the upper and lower interacting shells achieve the lattice fitting parameters by suiting the AB stacking [69,70].

The second mechanism which is attributed to the interactions of weak Van der Waals bonds can be elucidated with Van der Waals interactions with length-independence on the carbon shells. The repeated snaping1 and reforming of the Van der Waals bonds eliminates the average shear stress at the mating surfaces [71]. The frictional energy dissipation at the mating surfaces is, therefore, minimized.

The Raman spectroscopy and SEM results discussed earlier are linked to the coefficient of friction evolution curve (Fig. 10(fi-iv)). This reveals four stages of friction contact interactions during the wear process. The first stage (Fig. 10(fi)) is the plunging and coalescence stage (1000 cycles), where the multiwalled nanotubes and defective graphene structures break down and smear together to form the composite film with graphene oxide signatures in the wear track. The second stage (Fig. 10 (fii)) is the stabilized CoF regime with the cycles range of (10000–220,000 cycles).

The third stage (Fig. 10(fiii)) is characterized by breaking and removing the graphene composite films from the tracks due to intense wear action between the mating surfaces. This happens with the cycles range of ~220000 – ~330000 cycles. This leads to another plunging regime and an unstable regime where the CoF values rose to an average of 0.5 ± 0.3. The Raman spectra in this regime were associated with graphene nanocrystals structures. This represented the threshold for graphene protection as the wear mechanism transitioned to adhesive and abrasive wear. The final stage (Fig. 10(fiv)) is the total removal of the graphene composite film from the tracks (after 300,000 cycles) which is characterized by adhesion and abrasive wear with Fe_3O Raman signatures in the wear tracks.

The CoF value stabilized at ~0.17, sustained for 6000 s. The graphene composite film fully developed and covered most of the wear tracks. The Raman spectroscopy of the wear tracks still revealed graphene oxide structures.

The AFM analysis of the superlubricious wear tracks of the 900 HTBT substrates as presented in Fig. 11 reveals multiple nano- micro-contact

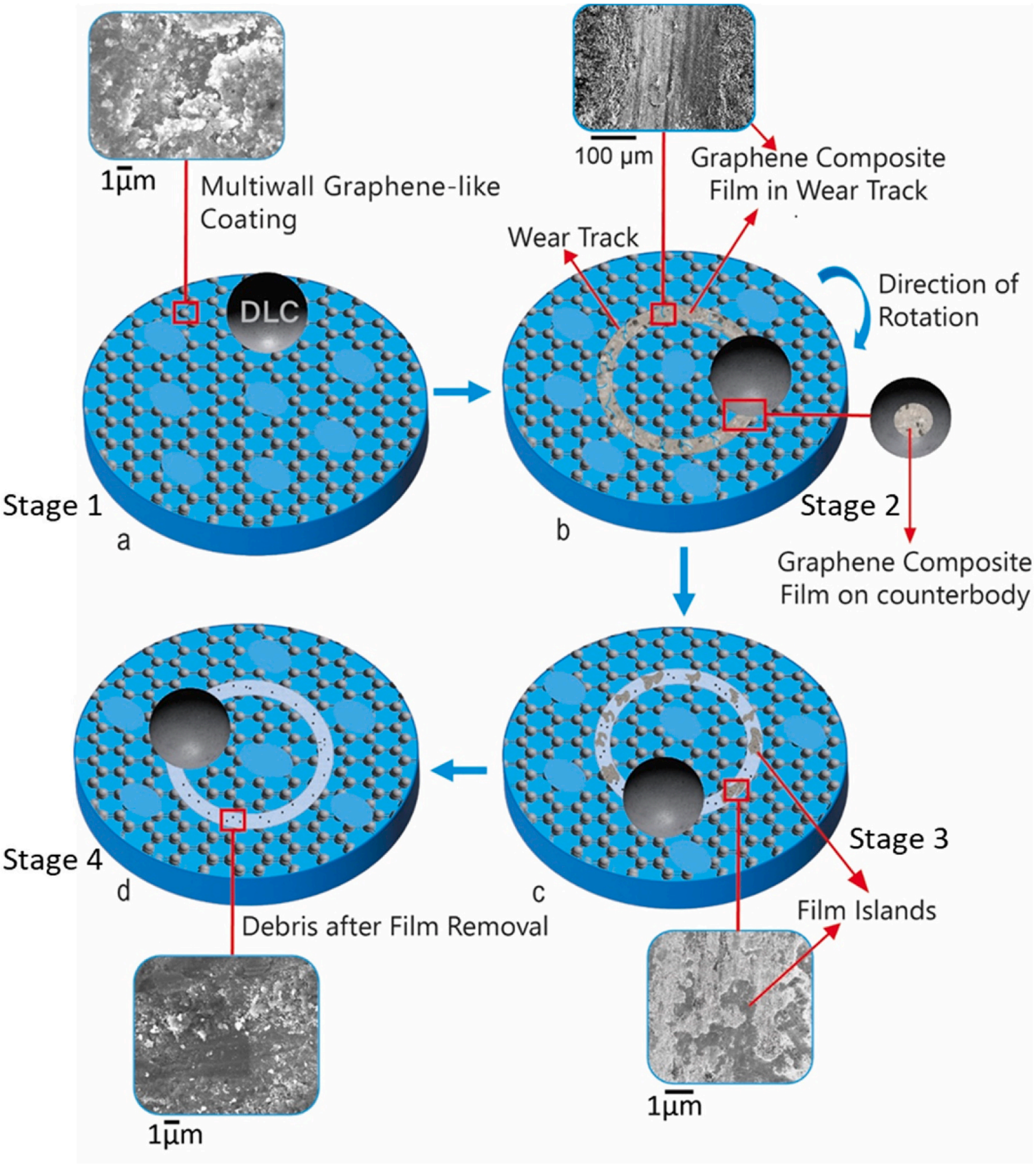

Fig. 12. Wear stages schematic showing; (a) Stage 1: multiwall graphene-like coating with patches on substrate and ball, (b) Stage 2: formed graphene nanocomposite film with cracks in the tracks and counter body, providing graphitic protection, (c) Stage 3: graphene nanocomposite film islands in the tracks due to continues scratching of the counter body, (d) Stage 4: wear debris in wear tracks after removal of protective carbon film.

points in them (Fig. 11 c and d). The root mean square roughness value of the 1000 cycles wear track was 146.3 ± 20.48 nm, which was reduced to 105.6 ± 9.5 nm for the 40,000 cycles wear tracks and led to the stabilized CoF value of ~0.0015 (as can be seen in Fig. 11e). The CoF values increased to above 0.1 with a root mean square roughness value of 250 nm after 40,000 cycles (Fig. 11e). The maximum peak on the 1000 cycles wear tracks was 1359 ± 271.9 nm and that on the 40,000 cycles wear track was 1262 ± 138.86 nm. Since the discovery of single nano contact point frictionless conditions, using friction force microscopy [59], it has been ascertained that multiple nano- micro-contact points of 2D materials will yield macroscale superlubricity, as seen in this work. Majority of the nano-contact points would to have been in the registry as superlubricious to yield an over frictionless condition.

Fig. 12 presents a schematic of the wear mechanism of the treated substrates. Fig. 12(a) shows the state of the substrates with the coating after the treatment. This figure shows the graphene-like coatings with patches in them. Fig. 12(b) represents the initial stages of the wear process of the treated substrates where the graphene nanocomposite films cover most parts of the wear tracks. This stage is characterized by low friction and wear as seen in Fig. 10. This stage also presents the composite film formation on ball. The evidence of the formation of the composite film on the substrate and ball have been presented in this work (Figs. 5, 7, and 9e). The ball used for the wear test was also treated with the HTBT process and had the carbon deposited on them. From the SEM and Raman investigations (Fig. 9) of the ball scar after 1000 s the graphene composite films were detected in them as well. This film formation on ball and substrate led to the film-on-film mechanism as described in this work. This mechanism as observed in prior work enables carbon-on-carbon interactions which is reported to result to superlubricious contacts [7,62,72].

Fig. 12(c) represents an advanced stage of the wear process where the graphene nanocomposite films have been removed to form islands in the wear tracks. Fig. 12(d) also represents the end stage of the wear process where all the carbon rich films have been removed from the wear tracks giving promoting adhesive and abrasive wear mechanisms. This stage was associated with high wear rates and CoF values.

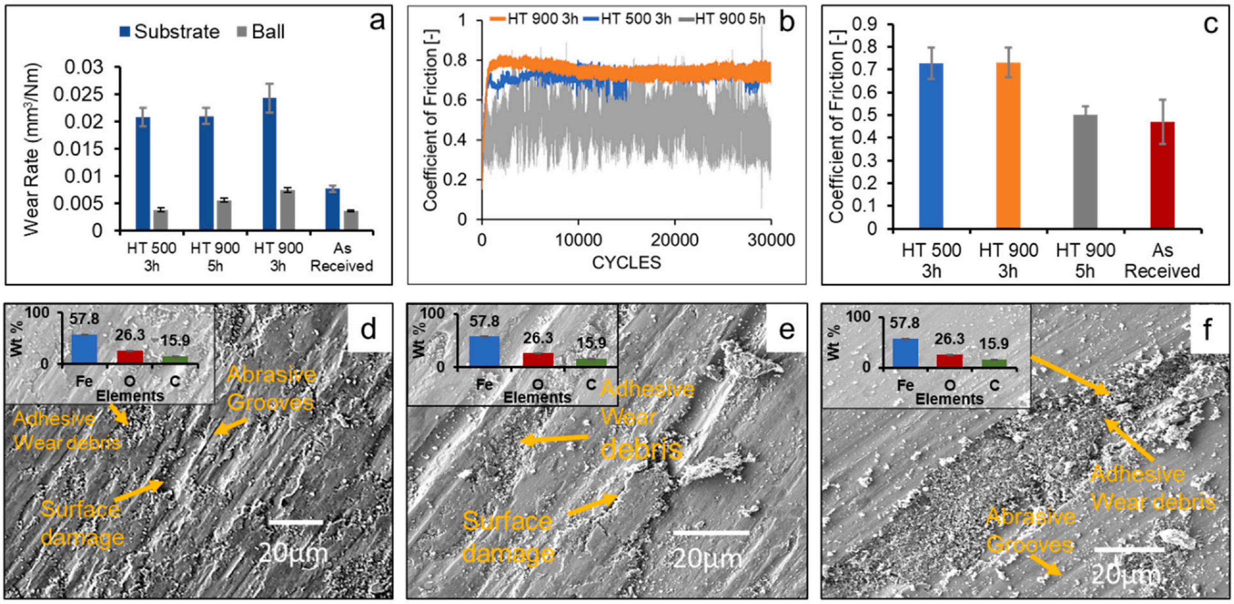

Fig. 13. Friction and wear results of heat treated AISI 1045 steel without the carbon coating; (a) wear rate results of substrates and ball, (b) Coefficient of friction versus cycles plot of the HT 500 3 h, HT 900 3 h and HT 900 5 h samples, (c) Average Coefficient of friction results for the various heat treated substrates as compared to the as-received steel, (d)–(f) SEM micrographs of the worn-out surfaces of the HT 500 3 h, HT 900 3 h and HT 900 5 h, respectively.

3.7. Implications

The main consequences of the ultralow friction and wear are enormous energy savings and increased wear life. This study presents initial results that suggest that these benefits can be achieved by our novel biotreatment method. The surface carbon coatings result in near-zero friction and wear in contact with metallic substrates such as the 1045 steel that was investigated and examined.

Fig. 13 compares friction and wear data for normalized (heat-treated) samples without a carbon coating, revealing how microstructural changes affect tribological behavior. The HT 500 3 h, HT 900 3 h, and HT 900 5 h samples exhibit wear rates of 0.0209 ± 0.00167, 0.0243 ± 0.00268, and 0.021 ± 0.00147 mm^3/Nm, respectively, all higher than the 0.0077 ± 0.00061 mm^3/Nm of the as-received. The respective counter bodies also show increased wear compared to the as-received steel. Consequently, normalizing without carbon coating worsens wear properties, underscoring that the biowaste treatment method greatly enhances wear life. Furthermore, the HT 500 3 h, HT 900 3 h, and HT 900 5 h samples show coefficients of friction of 0.727 ± 0.069, 0.731 ± 0.064, and 0.5 ± 0.039, respectively which are higher than the 0.47 ± 0.097 of the as-received (Fig. 13(b, c)). The stick-and-slide behavior is more pronounced in the HT 900 5 h sample (Fig. 13(b)). SEM images of wear tracks from the normalized control samples (Fig. 13(a–f)) reveal abrasive grooves, surface damage, and adhesive debris, indicating a similar wear mechanism to the as-received material.

The new low-cost biotreatment method was used to deposit multi-walled graphene-like coatings at 500°C and 900°C. This economical and innovative process has been shown to be effective, eliminating the need for expensive equipment or complex standard operating procedures. Frequently, companies can adopt and integrate this method into their existing hardening and softening treatments seamlessly. Conventional graphene deposition methods (CVD and PVD) rely on a carbon-based precursor (e.g., methane), high temperatures near 1000°C, hydrogen gas atmospheres, and specialized vacuum systems [73], leading to costs of about $300 per wafer [74]. In contrast, a new biotreatment approach uses dried and pulverized Manihot esculenta biowaste in a simple pack-cementation process within a standard furnace, reducing costs to around $20 per wafer. This method is scalable, requires only common laboratory equipment (e.g., muffle or Lenton furnaces), and avoids the need for vacuum or plasma technologies, making it significantly more cost-effective for large-scale applications.

This biotreatment method is associated with a circular economic model, in which biowaste is converted into valuable carbon sources for industrial applications. It also offers a way of decreasing the energy losses due to friction. Furthermore, the reduced wear rates of the carbon-coated surfaces are likely to improve the service lives and structural integrity of the superlubricated steel surfaces in engineering components and structures.

4. Summary and concluding remarks

1. The high temperature biowaste treatment method is a practical cost-effective method for depositing variants of graphene on AISI 1045 steel. The high temperature biowaste treatment was done at 500°C and 900°C. Characterizing the surfaces of the 500 HTBT substrates showed carbon nanocrystal deposition with increased concentration of carbon. The 900 HTBT substrates also had a high carbon concentration at the surface with multi-walled carbon nanotube and graphene platelet deposits (the graphene structures were confirmed with Raman microscopy) on the substrates. This was essential for inducing frictionless and ultra-low wear conditions on the treated substrates.
2. Distinct variations in the wear mechanisms were observed among the As-received, 500°C HTBT and 900°C HTBT substrates. For the As-received and 500 °C HTBT substrates, abrasive and adhesive wear mechanisms were observed throughout the test. However, after 1000 cycles of test on the 900°C HTBT substrates, SEM micrographs revealed a film in the wear tracks composed of graphene nanocrystals and graphene oxide, resulting from stress-induced graphitization and tribological-oxidation.
3. The wear rates of the substrates decreased by 76% for the 3 h treated 900 HTBT substrates, 88% for the 5 h treated 900 HTBT substrates, and 15% for the 3 h treated 500 HTBT substrates as compared to the untreated substrates. The wear rates for the counter body were also reduced by 96% for the 5 h 900 HTBT substrates, 95% for the 3 h 900 HTBT substrates and 27% for the 3 h treated 500 HTBT substrates as juxtaposed with that of the untreated substrates. The formation of graphene nanocomposite films as a protective layer in the wear

tracks were responsible for these reduction in wear rates on both substrates and counter body.

4. The 900 HTBT substrates ranked highest in the wear merit index evaluation of the substrates. Therefore, these coated substrates are the most preferred material for bearing and wear applications. The most suitable conditions for optimal wear properties for the treatment of steels will therefore be 900°C for at least 3 h.
5. Macroscale superlubricity of CoF value 0.0015 was attained in this work. This was achieved on the substrates that were treated for 5 h at 900°C. The CoF values of the treated substrates were decreased by 95.20% for the 5 h 900HTBT substrates, 77.08% for the 900 HTBT substrates treated for 3 h, and 29.17 % for the 500 HTBT substrates that were treated for 3 h. The low CoF conditions were sustained for at least 220,000 cycles before transitioning to the original CoF values of the untreated substrates. This marked the end of the graphene protection.
6. This biotreatment method, therefore, offers an economical and simple method of attaining scalable ultra-low friction, enhanced microhardness and decreased wear rates with prolonged wear life of coatings on steel and other metals. These are essential for achieving sustained solid lubrication in materials.

CRediT authorship contribution statement

Tabiri Kwayie Asumadu: Writing – review & editing, Writing – original draft, Visualization, Methodology, Investigation, Formal analysis, Data curation, Conceptualization. **Mobin Vandadi:** Writing – review & editing, Writing – original draft, Visualization, Validation, Software, Methodology, Conceptualization. **Desmond Edem Primus Klenam:** Writing – review & editing, Writing – original draft, Investigation, Formal analysis, Conceptualization. **Kwadwo Mensah-Darkwa:** Writing – review & editing, Supervision, Conceptualization. **Kwadwo Adinkrah-Appiah:** Writing – review & editing, Funding acquisition, Conceptualization. **Emmanuel Gikunoo:** Writing – review & editing, Supervision, Conceptualization. **Nima Rahbar:** Writing – review & editing, Supervision, Software, Formal analysis, Conceptualization. **Samuel Kwofie:** Writing – review & editing, Supervision, Conceptualization. **Winston Oluwole Soboyejo:** Writing – review & editing, Supervision, Project administration, Funding acquisition, Conceptualization.

Declaration of competing interest

The authors declare that they have no known competing financial interests or personal relationships that could have appeared to influence the work reported in this paper.

Acknowledgements

The authors are grateful to the SUNY Polytechnic Institute (SUNY Poly) and the Global Fund of the Worcester Polytechnic Institute for financial support.

Data availability

The research data includes sensitive information but can be made available upon the signing of appropriate non-disclosure agreements.

References

[1] O. Hod, E. Meyer, Q. Zheng, M. Urbakh, Structural superlubricity and ultralow friction across the length scales, Nature 563 (2018) 485–492, https://doi.org/10.1038/s41586-018-0704-z.

[2] S.P. Brühl, A. Cabo, W. Tuckart, G. Prieto, Tribological behaviour of nitrided and nitrocarburized carbon steel used to produce engine parts, Ind. Lubr. Tribol. 68 (2016) 125–133, https://doi.org/10.1108/ILT-07-2015-0101.

[3] A. Çelik, M. Karakan, A. Alsaran, I. Efeoglu, The investigation of structural, mechanical and tribological properties of plasma nitrocarburized AISI 1020 steel, Surf. Coat Technol. 200 (2005) 1926–1932, https://doi.org/10.1016/j.surfcoat.2005.08.027.

[4] D.E.P. Klenam, T.K. Asumadu, M. Vandadi, N. Rahbar, F. McBagonluri, W. O. Soboyejo, Data science and material informatics in physical metallurgy and material science: an overview of milestones and limitations, Results Mater. 19 (2023) 100455, https://doi.org/10.1016/j.rinma.2023.100455.

[5] S.A. Osafo, P.O. Etinosa, J.D. Obayemi, A.A. Salifu, T. Asumadu, D. Klenam, B. Agyei-Tuffour, D. Dodoo-Arhin, A. Yaya, W.O. Soboyejo, Hydroxyapatite nanopillars on <scp>TI-6Al-4V</scp>: enhancements in cell spreading and proliferation during cell/surface integration, J. Biomed. Mater. Res. A (2024), https://doi.org/10.1002/jbm.a.37726.

[6] H.P. Mungse, O.P. Khatri, Chemically functionalized reduced graphene oxide as a novel material for reduction of friction and wear, J. Phys. Chem. C 118 (2014) 14394–14402, https://doi.org/10.1021/jp5033614.

[7] P. Wu, X. Li, C. Zhang, X. Chen, S. Lin, H. Sun, C.-T. Lin, H. Zhu, J. Luo, Self-assembled graphene film as low friction solid lubricant in macroscale contact, ACS Appl. Mater. Interfaces 9 (2017) 21554–21562, https://doi.org/10.1021/acsami.7b04599.

[8] M. Wang, H. Liu, Y. Wang, K. Hou, J. Wang, S. Yang, Stable lubrication in air and vacuum of GO-Al3+ coating via strong chemical bonding and reactive sites passivation by aluminum ions, Carbon N. Y. 160 (2020) 247–254, https://doi.org/10.1016/j.carbon.2019.12.098.

[9] J. Liu, X. Wang, Y. Liu, X. Liu, K. Fan, Bioinspired three-dimensional and multiple adsorption effects toward high lubricity of solvent-free graphene-based nanofluid, Carbon N. Y. 188 (2022) 166–176, https://doi.org/10.1016/j.carbon.2021.11.065.

[10] T. Bartels, W. Bock, J. Braun, C. Busch, W. Buss, W. Dresel, C. Freiler, M. Harperscheid, R.-P. Heckler, D. Hörner, F. Kubicki, G. Lingg, A. Losch, R. Luther, T. Mang, S. Noll, J. Omeis, in: Ullmann's Encyclopedia of Industrial Chemistry, Wiley-VCH Verlag GmbH & Co. KGaA, Weinheim, Germany, 2003, https://doi.org/10.1002/14356007.a15_423.

[11] C. Chen, P. Xue, D. Diao, Graphitization vs tribo-oxidation governing friction behaviors of doped graphene nanocrystalline carbon films, Carbon N. Y. 197 (2022) 435–443, https://doi.org/10.1016/j.carbon.2022.07.001.

[12] M. Wang, Z. Li, J. Wang, S. Yang, Iron ions induced self-assembly of graphene oxide lubricating coating with self-adapting low friction characteristics, Carbon N. Y. 201 (2023) 1151–1159, https://doi.org/10.1016/j.carbon.2022.10.013.

[13] M.M. Al-Asadi, H.A. Al-Tameemi, A review of tribological properties and deposition methods for selected hard protective coatings, Tribol. Int. 176 (2022), https://doi.org/10.1016/j.triboint.2022.107919.

[14] X. Chen, J. Li, Superlubricity of carbon nanostructures, Carbon N. Y. 158 (2020) 1–23, https://doi.org/10.1016/j.carbon.2019.11.077.

[15] Y. Meng, J. Xu, L. Ma, Z. Jin, B. Prakash, T. Ma, W. Wang, A review of advances in tribology in 2020–2021, Friction 10 (2022) 1443–1595, https://doi.org/10.1007/s40544-022-0685-7.

[16] D. Berman, A. Erdemir, A.V. Sumant, Graphene: a new emerging lubricant, Mater. Today 17 (2014) 31–42, https://doi.org/10.1016/j.mattod.2013.12.003.

[17] A.K. Geim, I.V. Grigorieva, Van der Waals heterostructures, Nature 499 (2013) 419–425, https://doi.org/10.1038/nature12385.

[18] D. Berman, S.A. Deshmukh, S.K.R.S. Sankaranarayanan, A. Erdemir, A.V. Sumant, Macroscale superlubricity enabled by graphene nanoscroll formation, Science 348 (2015) (1979) 1118–1122, https://doi.org/10.1126/science:1262024.

[19] Y. Liu, Z. Fan, S. Yu, R. Zhang, J. Zhang, T.W. Liskiewicz, X. Ge, W. Wang, Macroscale structural superlubricity: dynamic evolution of tribolayers in two-dimensional materials under extreme pressure, Nano Energy 129 (2024) 110072, https://doi.org/10.1016/j.nanoen.2024.110072.

[20] G. Yu, W. Chen, H. Wang, W. Tang, Z. Gong, Effects of relative humidities on the superlubricity of GO/MoS2/H-DLC triple composite, Diam. Relat. Mater. 148 (2024) 111444, https://doi.org/10.1016/j.diamond.2024.111444.

[21] T. Sun, E. Gao, X. Jia, J. Bian, Z. Wang, M. Ma, Q. Zheng, Z. Xu, Robust structural superlubricity under gigapascal pressures, Nat. Commun. 15 (2024) 5952, https://doi.org/10.1038/s41467-024-49914-6.

[22] H. Li, Q. Wang, P. Xu, L. Si, Z. Dou, H. Yan, Y. Yang, G. Zhou, T. Qing, S. Zhang, F. Liu, Structural superlubricity in graphene/GaSe van der Waals heterostructure, Phys. Lett. A 452 (2022) 128435, https://doi.org/10.1016/j.physleta.2022.128435.

[23] Q. Jia, Z. Yang, B. Zhang, K. Gao, L. Sun, J. Zhang, Macro superlubricity of two-dimensional disulphide/amorphous carbon heterogeneous via tribochemistry, Mater. Today Nano 21 (2023) 100286, https://doi.org/10.1016/j.mtnano.2022.100286.

[24] X. Ge, Z. Chai, Q. Shi, Y. Liu, W. Wang, Graphene superlubricity: a review, Friction 11 (2023) 1953–1973, https://doi.org/10.1007/s40544-022-0681-y.

[25] S. Fan, Y. Chen, J. Wu, S. Xiao, G. Chen, P.K. Chu, Structure, superlubricity, applications, and chemical vapor deposition methods of graphene solid lubricants, Tribol. Int. 198 (2024) 109896, https://doi.org/10.1016/j.triboint.2024.109896.

[26] T.K. Asumadu, M. Vandadi, D.E.P. Klenam, K. Mensah-Darkwa, E. Gikunoo, S. Kwofie, N. Rahbar, W.O. Soboyejo, Robust macroscale superlubricity on carbon-coated metallic surfaces, Appl. Mater. Today 37 (2024), https://doi.org/10.1016/j.apmt.2024.102140.

[27] B. Addai, K.O. Gyimah, T.K. Asumadu, M. Anto, D.E.P. Klenam, W.O. Soboyejo, Strain gradient plasticity in AISI A36 plain carbon steel weldment: comparison of butt and lap joint configurations, Results Eng. 22 (2024) 102078, https://doi.org/10.1016/j.rineng.2024.102078.

[28] E.K. Arthur, S.T. Azeko, Surface hardening of ferrous materials with cassava (Manihot spp.) waste: a review, Sci. Afr. 9 (2020), https://doi.org/10.1016/j.sciaf.2020.e00483.

[29] E.K. Ampaw, E.K. Arthur, O.O. Adewoye, A.R. Adetunji, S.O.O. Olusunle, W. O. Soboyejo, Carbonitriding "Pack Cyaniding" of Ductile Irons, Adv. Mat. Res. 1132 (2015) 330–348, https://doi.org/10.4028/www.scientific.net/amr.1132.330.

[30] E.K. Arthur, E. Ampaw, K.J. Akinluwade, A.R. Adetunji, O.O. Adewoye, W. O. Soboyejo, Carbon and nitrogen concentration profiles of cassava-pack carbonitrided steel: model and experiment, Adv. Mater. Res. 1132 (2015) 313–329, https://doi.org/10.4028/www.scientific.net/amr.1132.313.

[31] X. Zhu, L. Lin, M. Pang, C. Jia, L. Xia, G. Shi, S. Zhang, Y. Lu, L. Sun, F. Yu, J. Gao, Z. He, X. Wu, A. Li, L. Wang, M. Wang, K. Cao, W. Fu, H. Chen, G. Li, J. Zhang, Y. Wang, Y. Yang, Y.-G. Zhu, Continuous and low-carbon production of biomass flash graphene, Nat. Commun. 15 (2024) 3218, https://doi.org/10.1038/s41467-024-47603-y.

[32] P. Thibaux, A. Métenier, C. Xhoffer, Carbon diffusion measurement in austenite in the temperature range 500 °C to 900 °C, Metall. Mater. Trans. A 38 (2007) 1169–1176, https://doi.org/10.1007/s11661-007-9150-5.

[33] T.K. Asumadu, K. Mensah-Darkwa, E. Gikunoo, D.E.P. Klenam, M. Vandadi, N. Rahbar, S. Kwofie, W.O. Soboyejo, Strain gradient plasticity phenomenon in surface treated plain carbon steel, Mater. Sci. Eng. A 871 (2023) 144806, https://doi.org/10.1016/j.msea.2023.144806.

[34] S. Qin, C. Zhang, B. Zhang, H. Ma, M. Zhao, Effect of carburizing process on high cycle fatigue behavior of 18CrNiMo7-6 steel, J. Mater. Res. Technol. 16 (2022) 1136–1149, https://doi.org/10.1016/j.jmrt.2021.12.074.

[35] Supriyono, Jamasri, Holding time effect of pack carburizing on fatigue characteristic of v-notch shaft steel specimens, in: AIP Conf Proc, American Institute of Physics Inc., 2017. https://doi.org/10.1063/1.4985450.

[36] Z. Sun, D. Hou, W. Li, Effect of carburizing and nitriding on fatigue properties of 18Cr2Ni4WA steel in very high cycle fatigue regime, Ann. Chim. Sci. Mater. 45 (2021) 207–215, https://doi.org/10.18280/acsm.450303.

[37] S.E. Offerman, L.J.G.W. van Wilderen, N.H. van Dijk, J. Sietsma, M.T. Rekveldt, S. van der Zwaag, In-situ study of pearlite nucleation and growth during isothermal austenite decomposition in nearly eutectoid steel, Acta Mater. 51 (2003) 3927–3938, https://doi.org/10.1016/S1359-6454(03)00217-9.

[38] C. Zener, Kinetics of the decomposition of austenite, Trans. AIME 167 (1945) 550–595.

[39] D. Centeno, G. Tressia, F.M. Carvalho, F.E. Marques Cezario, E.A. Ariza, M. Masoumi, Enhancing mechanical properties and wear resistance of heavy-haul rail systems through complex microstructure control, J. Mater. Res. Technol. 27 (2023) 1146–1159, https://doi.org/10.1016/j.jmrt.2023.10.004.

[40] F. Zhang, T. Zhang, H. Gou, S. Chen, D. Wu, H. Wei, X. Chong, Z. Li, X. Wu, Q. Shan, Improving the impact wear properties of medium carbon steel by adjusting microstructure under alternating quenching in water and air, Wear 512–513 (2023) 204531, https://doi.org/10.1016/j.wear.2022.204531.

[41] D. Edem Primus Klenam, Composition refinement of medium carbon-low alloy steels to improve wear and corrosion resistance for rail axle applications, 2019.

[42] K. Zhang, X. Zhang, H. Li, X. Xing, L. Jin, Q. Cao, P. Li, Direct exfoliation of graphite into graphene in aqueous solution using a novel surfactant obtained from used engine oil, J. Mater. Sci. 53 (2018) 2484–2496, https://doi.org/10.1007/s10853-017-1729-7.

[43] X. Gao, T. Hiraoka, S. Ohmagari, S. Tanaka, Z. Sheng, K. Liu, M. Xu, P. Chen, K. Hokamoto, High-efficiency production of large-size few-layer graphene platelets via pulsed discharge of graphite strips, Nanomaterials 9 (2019) 1785, https://doi.org/10.3390/nano9121785.

[44] A. Bajorek, B. Szostak, M. Dulski, J.-M. Greneche, S. Lewińska, B. Liszka, M. Pawlyta, A. Ślawska-Waniewska, A comprehensive study of pristine and calcined f-MWCNTs functionalized by nitrogen-containing functional groups, Materials 15 (2022) 977, https://doi.org/10.3390/ma15030977.

[45] R. Siburian, H. Sihotang, S. Lumban Raja, M. Supeno, C. Simanjuntak, New route to synthesize of graphene nano sheets, Orient. J. Chem. 34 (2018) 182–187, https://doi.org/10.13005/ojc/340120.

[46] N.A. Mohd Zaid, N.H. Idris, Enhanced capacitance of hybrid layered graphene/nickel nanocomposite for supercapacitors, Sci. Rep. 6 (2016) 32082, https://doi.org/10.1038/srep32082.

[47] H. Zahlan, W.S. Saeed, S. Alqahtani, T. Aouak, Separation of benzene/cyclohexane mixtures by pervaporation using poly (ethylene-co-vinylalcohol) and carbon nanotube-filled poly (vinyl alcohol-co-ethylene) membranes, Separations 7 (2020) 68, https://doi.org/10.3390/separations7040068.

[48] M. Farbod, S.K. Tadavani, A. Kiasat, Surface oxidation and effect of electric field on dispersion and colloids stability of multiwalled carbon nanotubes, Colloids Surf. A Physicochem. Eng. Asp. 384 (2011) 685–690, https://doi.org/10.1016/j.colsurfa.2011.05.041.

[49] E.K. Arthur, E. Ampaw, M.G. Zebaze Kana, A.R. Adetunji, O.O. Adewoye, W. O. Soboyejo, Surface hardening of AISI 8620 steel with cassava (Manihot spp.) waste, Waste Biomass Valoriz. 7 (2016) 603–614, https://doi.org/10.1007/s12649-016-9479-3.

[50] G. Cruz, A.d.L.P. Rodrigues, D.F.d. Silva, W.C. Gomes, Physical–chemical characterization and thermal behavior of cassava harvest waste for application in thermochemical processes, J. Therm. Anal. Calorim. 143 (2021) 3611–3622, https://doi.org/10.1007/s10973-020-09330-6.

[51] L. Bokobza, J. Zhang, Raman spectroscopic characterization of multiwall carbon nanotubes and of composites, Express Polym. Lett. 6 (2012) 601–608, https://doi.org/10.3144/expresspolymlett.2012.63.

[52] A.C. Ferrari, D.M. Basko, Raman spectroscopy as a versatile tool for studying the properties of graphene, Nat. Nanotechnol. 8 (2013) 235–246, https://doi.org/10.1038/nnano.2013.46.

[53] A.C. Ferrari, Raman spectroscopy of graphene and graphite: disorder, electron-phonon coupling, doping and nonadiabatic effects, Solid State Commun. 143 (2007) 47–57, https://doi.org/10.1016/j.ssc.2007.03.052.

[54] A.C. Ferrari, J. Robertson, Interpretation of Raman spectra of disordered and amorphous carbon, Phys. Rev. B 61 (2000) 14095–14107, https://doi.org/10.1103/PhysRevB.61.14095.

[55] A.C. Ferrari, J.C. Meyer, V. Scardaci, C. Casiraghi, M. Lazzeri, F. Mauri, S. Piscanec, D. Jiang, K.S. Novoselov, S. Roth, A.K. Geim, Raman spectrum of graphene and graphene layers, Phys. Rev. Lett. 97 (2006), https://doi.org/10.1103/PhysRevLett.97.187401.

[56] A. Chouhan, H.P. Mungse, O.P. Khatri, Surface chemistry of graphene and graphene oxide: a versatile route for their dispersion and tribological applications, Adv. Colloid Interface Sci. 283 (2020) 102215, https://doi.org/10.1016/j.cis.2020.102215.

[57] Y. Zhang, F. Liang, Y. Lin, X. Chen, Y. Zhu, Mitigating friction and wear by pre-designed or tribo-induced heterostructures: an overview, Mater. Res. Lett. 12 (2024) 535–550, https://doi.org/10.1080/21663831.2024.2356282.

[58] M. Ghazinejad, S. Holmberg, O. Pilloni, L. Oropeza-Ramos, M. Madou, Graphitizing non-graphitizable carbons by stress-induced routes, Sci. Rep. 7 (2017), https://doi.org/10.1038/s41598-017-16424-z.

[59] M. Dienwiebel, G.S. Verhoeven, N. Pradeep, J.W.M. Frenken, J.A. Heimberg, H. W. Zandbergen, Superlubricity of graphite, Phys. Rev. Lett. 92 (2004), https://doi.org/10.1103/PhysRevLett.92.126101.

[60] R. Zhang, Z. Ning, Y. Zhang, Q. Zheng, Q. Chen, H. Xie, Q. Zhang, W. Qian, F. Wei, Superlubricity in centimetres-long double-walled carbon nanotubes under ambient conditions, Nat. Nanotechnol. 8 (2013) 912–916, https://doi.org/10.1038/nnano.2013.217.

[61] S. Jang, A.G. Colliton, H.S. Flaih, E.M.K. Irgens, L.J. Kramarczuk, G.D. Rauber, J. Vickers, A.L. Ogrinc, Z. Zhang, Z. Gong, Z. Chen, B.P. Borovsky, S.H. Kim, Why is superlubricity of diamond-like carbon rare at nanoscale? Small 20 (2024) https://doi.org/10.1002/smll.202400513.

[62] Y. Liu, H. Zhang, Roles of transfer layer and surface adhesion on superlubricity behaviors of diamond-like carbon film depending on rotating and reciprocating motion, Appl. Surf. Sci. 604 (2022) 154538, https://doi.org/10.1016/j.apsusc.2022.154538.

[63] H. Algul, M. Tokur, S. Ozcan, M. Uysal, T. Cetinkaya, H. Akbulut, A. Alp, The effect of graphene content and sliding speed on the wear mechanism of nickel–graphene nanocomposites, Appl. Surf. Sci. 359 (2015) 340–348, https://doi.org/10.1016/j.apsusc.2015.10.139.

[64] B. Jiang, Z. Zhao, Z. Gong, D. Wang, G. Yu, J. Zhang, Superlubricity of metal-metal interface enabled by graphene and MoWS4 nanosheets, Appl. Surf. Sci. 520 (2020) 146303, https://doi.org/10.1016/j.apsusc.2020.146303.

[65] W.-W. Yao, X.-P. Zhou, D. Dias, Y. Jia, Y.-J. Li, Frictional contact and stick-slip: mechanism and numerical technology, Int. J. Solids Struct. 274 (2023) 112289, https://doi.org/10.1016/j.ijsolstr.2023.112289.

[66] A. Vanossi, C. Bechinger, M. Urbakh, Structural lubricity in soft and hard matter systems, Nat. Commun. 11 (2020) 4657, https://doi.org/10.1038/s41467-020-18429-1.

[67] M. Liao, P. Nicolini, L. Du, J. Yuan, S. Wang, H. Yu, J. Tang, P. Cheng, K. Watanabe, T. Taniguchi, L. Gu, V.E.P. Claerbout, A. Silva, D. Kramer, T. Polcar, R. Yang, D. Shi, G. Zhang, UItra-low friction and edge-pinning effect in large-lattice-mismatch van der Waals heterostructures, Nat. Mater. 21 (2022) 47–53, https://doi.org/10.1038/s41563-021-01058-4.

[68] D. Berman, A. Erdemir, Achieving ultralow friction and wear by tribocatalysis: enabled by *in-operando* formation of nanocarbon films, ACS Nano 15 (2021) 18865–18879, https://doi.org/10.1021/acsnano.1c08170.

[69] A. Erdemir, Superlubricity, second ed., Elsevier, 2020.

[70] Z. Liu, J. Yang, F. Grey, J.Z. Liu, Y. Liu, Y. Wang, Y. Yang, Y. Cheng, Q. Zheng, Observation of microscale superlubricity in graphite, Phys. Rev. Lett. 108 (2012) 205503, https://doi.org/10.1103/PhysRevLett.108.205503.

[71] Y. Li, N. Hu, G. Yamamoto, Z. Wang, T. Hashida, H. Asanuma, C. Dong, T. Okabe, M. Arai, H. Fukunaga, Molecular mechanics simulation of the sliding behavior between nested walls in a multi-walled carbon nanotube, Carbon N. Y. 48 (2010) 2934–2940, https://doi.org/10.1016/j.carbon.2010.04.031.

[72] A. Erdemir, O. Eryilmaz, Achieving superlubricity in DLC films by controlling bulk, surface, and tribochemistry, Friction 2 (2014) 140–155, https://doi.org/10.1007/s40544-014-0055-1.

[73] J. Nam, J. Yang, Y. Zhao, K.S. Kim, Chemical vapor deposition of graphene and its characterizations and applications, Curr. Appl. Phys. 61 (2024) 55–70, https://doi.org/10.1016/j.cap.2024.02.010.

[74] A. Alghfeli, T.S. Fisher, Sequential Bayesian-optimized graphene synthesis by direct solar-thermal chemical vapor deposition, Sci. Rep. 14 (2024) 3660, https://doi.org/10.1038/s41598-024-54005-z.